運輸省港湾技術研究所 (25th Anniversary Issue)

港湾技術研究所報告

REPORT OF THE PORT AND HARBOUR RESEARCH INSTITUTE

MINISTRY OF TRANSPORT

VOL. 26 NO. 5 DEC. 1987

NAGASE, YOKOSUKA, JAPAN

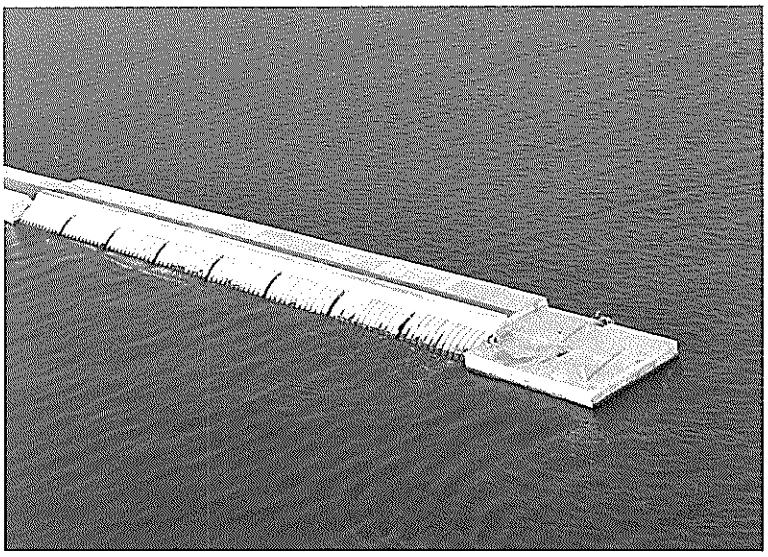

Curved Slit Caisson Breakwater

View of curved slit caisson breakwater completed in the construction at the port of Funakawa. (Courtesy of Akita Port Construction Office, the First District Port Construction Bureau, Ministry of Transport)

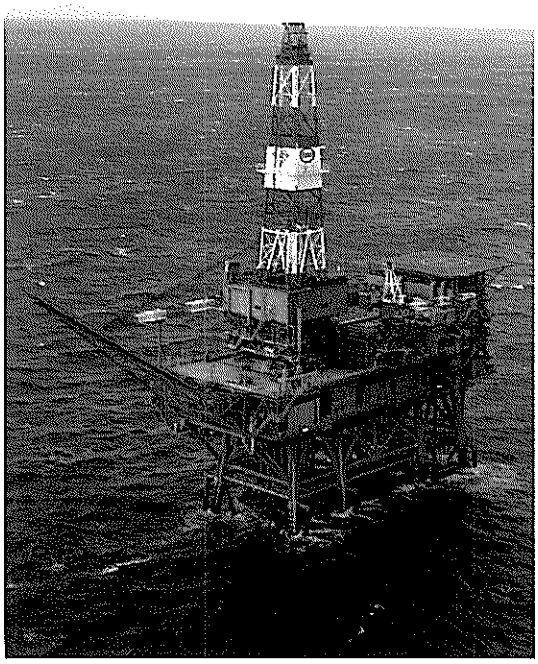

Facilities for Ocean Directional Wave Measurement

Four step type wave gauges and a two-axis directional current meter with a pressure sensor are installed on the legs of an offshore oil rig. They are operated simultaneously for detailed directional wave analysis.

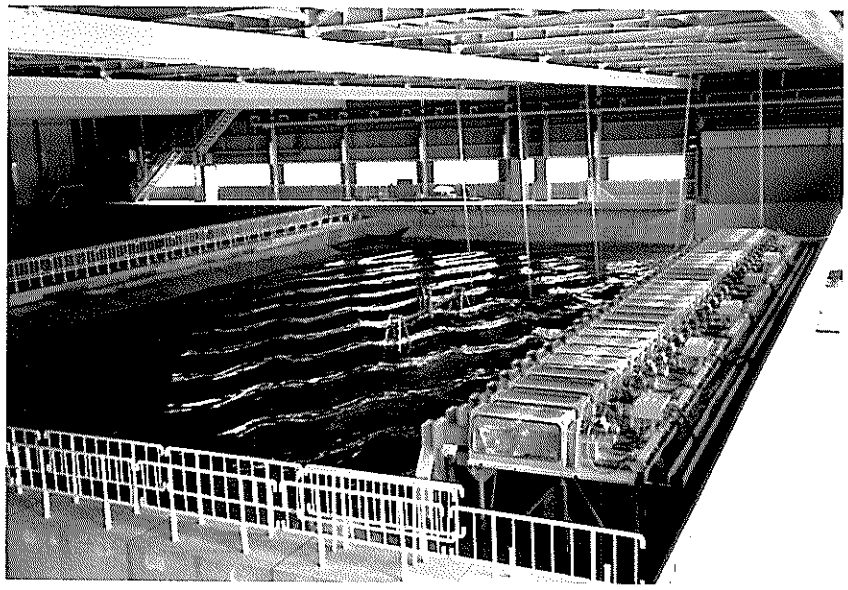

Serpent-type Wave Generator

The photograph shows the serpent-type wave generator in the short-crested wave basin and the superimposition state of two different oblique waves generated by the generator.

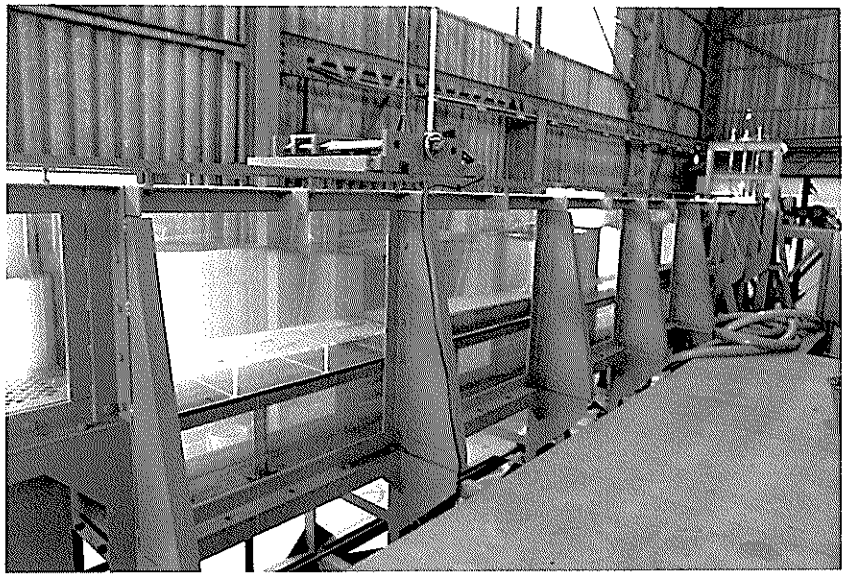

Wave-soil Tank

The experiments concerning the wave-soil interactions are conducted in this tank. The soil tank and the test section are located at the center of the tank. A movable floor is provided at the bottom of the test section and the level of the interface of mud layer and water can easily be adjusted to the level of the flume bottom.

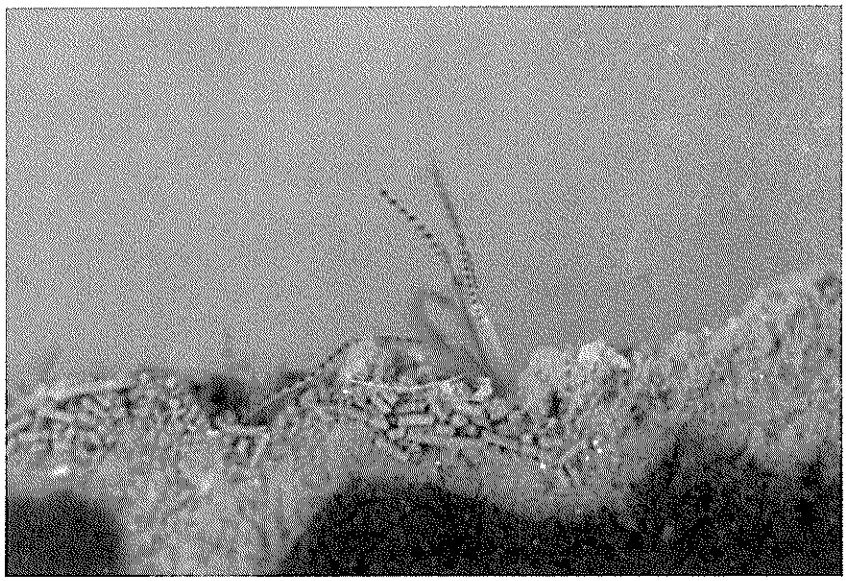

Pararionospio Pinnata

The biomass of benthos is one of the most sensitive indices to know the effect of sea-bed sediment treatments on the marine environmental improvement. The picure shows a kind of benthos, *pararionospio pinnata,* which preferentially exists in the polluted sea-bed.

Breakwater Damaged by Storm

This photograph shows a breakwater damage by a storm.
The breakwater is of the composite type with concrete caisson on a rubble mound. Two caissons were severly damaged due to the instability of a rubble mound.

Nondestructive Evaluation of Pavement

Nondestructive methods for evaluating the load carrying capacity of airport concrete pavements have been developed by using Falling Weight Deflectometer(FWD).

Seismic Damage to Gravity Quaywall

The 1983 Nipponkai-Chubu earthquake(Magnitude : 7.7)caused serious damage to port facilities in northern part of Japan. This photo shows the damage to gravity quaywall. The concrete cellular block walls were collapsed and completely submerged.

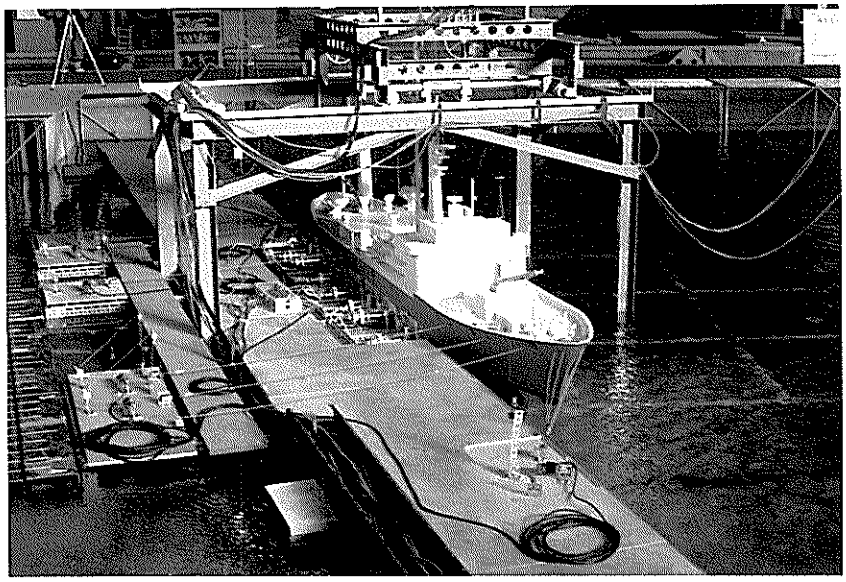

Model Experiment of Mooring Ship

Model ship is moored at a quay wall with fenders and mooring ropes subjected to gusty wind and/or irregular waves.

Vessel Congestion in Japan

As Japan is surrounded by the sea, there are many crowded water areas with various sizes and types of vessels. Arround there, many construction works were planned such as ports and harbours, off-shore airports, huge bridges and so on, so that many marine traffic observations and marine traffic simulations have been carried out.

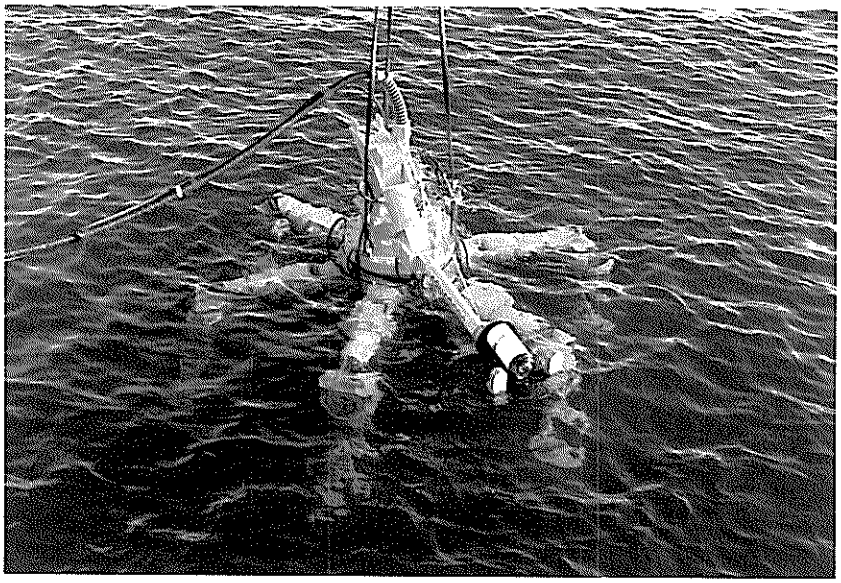

Underwater Inspection Robot

This is the six-legged articulated underwater inspection robot named "AQUAROBOT". The robot controlled by a computer can walk on uneven sea bed without making water muddy.

Foreword

The Port and Harbour Research Institute is a national laboratory under the Ministry of Transport, Japan. It is responsible for solving various engineering problems related to port and harbour projects so that governmental agencies in charge of port development can execute the projects smoothly and rationally. Its research activities also cover the studies on civil engineering facilities of air ports.

Last April we have celebrated the 25th anniversary of our institute because the present organization was established in 1962, though systematic research works on ports and harbours under the Ministry of Transport began in 1946. As an event for the celebration, we decided to publish a special edition of the Report of the Port and Harbour Research Institute, which contains full English papers only. These papers are so selected to introduce the versatility of our activities and engineering practices in Japan to overseas engineers and scientists. It is also intended to remedy to a certain extent the information gap between overseas colleagues and us.

The reader will find that our research fields cover physical oceanography, coastal and ocean engineering, geotechnical engineering, earthquake engineering, materials engineering, dredging technology and mechanical engineering, planning and systems analysis, and structural analysis. Such an expansion of the scope of research fields has been inevitable, because we are trying to cover every aspect of technical problems of ports and harbours as an integrated body.

The present volume contains eleven papers representing six research divisions of the institute. The materials introduced in these papers are not necessarily original in strict sense, as some parts have been published in Japanese in the Reports or the Technical Notes of the Port and Harbour Research Institute. Nevertheless they are all original papers in English and are given the full format accordingly. We expect that they will be referred to as usual where they deserve so.

It is my sincere wish that this special edition of the Report of the Port and Harbour Research Institute will bring overseas engineers and scientists more acquainted with our research activities and enhance the mutual cooperation for technology development related to ports and harbours.

December 1987
Yoshimi Goda
Director General

港湾技術研究所報告 (REPORT OF P. H. R. I.)
第26巻 第5号 (Vol. 26, No. 5) 1987年12月 (Dce. 1987)

目　　次 (CONTENTS)

REPORT OF THE PORT AND
HARBOUR RESEARCH INSTITUTE
Vol. 26, No. 5 (Dec. 1987)

3. Fundamental Characteristics of Oblique Regular Waves and Directional Random Waves Generated by a Serpent-type Wave Generator

Tomotsuka TAKAYAMA*
Tetsuya HIRAISHI**

Synopsis

For long time coastal engineers have wanted to reproduce directional random waves similar to sea waves, in their laboratory basins. Recently, several hydraulic research institutes in the world, including our institute, have built serpent-type wave generators which can generate the directional random waves by the motions of segmented wave paddles.

The present paper has discussed the properties of the oblique regular waves and directional random waves generated by segmented wave generators. The theoretical formula for the oblique waves has been derived as the linear superimposition of waves radiated by the motion of each segmented wave paddle. The properties of the oblique waves are investigated by experiments and numerical computations, and experiments have confirmed the validity of the formula.

The cross-spectrum has been obtained theoretically from the formula of oblique waves, and the examinations of the cross-spectrum of directional random waves have yielded the conclusions that two different representations of the single and double summation models are equivalent to each other, as long as the number of frequency components in the simulation of wave generation signals is sufficiently large. To eliminate the effect of phase locking in the double summation model, the number of frequency components needs to be more than 450.

The spatial variability of the directional spreading function has been investigated by using the Bayesian model as an estimation method for directional spectra. When the observation points of directional random waves are transversely moved from the center line of the wave generator, the directional spreading curve is distorted from the target and becomes asymmetric to the principal direction.

For the value of the directional concentration parameter of $S_{max}=25$, the experimentally observed directional spreading function agrees well with theoretically computed ones, but for other values of S_{max}, their agreement is not good. One of main causes of the disagreement seems due to the insufficient number of frequency components in the simulation of wave generation signals.

* Chief of the Wave Laboratory, Marine Hydrodynamics Division
** Member of the Wave Laboratory, Marine Hydrodynamics Division

港湾技術研究所報告
第26巻 第5号 (1987.12)

3. サーペント型造波機で起した斜め波と多方向不規則波の特性

高山知司*・平石哲也**

要旨

多方向不規則波を実験水槽内に起し，実際の海の波に近い状態で模型実験を行うことは海岸・港湾技術者の長い間の念願であった。近年になって，世界のいくつかの研究所では，造波板幅の狭い数多くの造波機を一直線上に並べて，多方向不規則波を起すサーペント型造波機を設置するようになってきた。港湾技術研究所においても昭和58年度からサーペント型造波機の建設を始め，昭和61年度に完成させた。

本論文においては，サーペント型造波機で起した斜め波や多方向不規則波の特性について理論的および実験的に検討した結果について述べている。

まず，一台一台の造波機によって起される波を線型的に重ね合わせることによって，サーペント型造波機で起した斜め波の理論式を導き，実験と比較することによってその式の妥当性を確認した。

つぎに，斜め波の理論式を用いて，数個の計算点間のクロススペクトルを求め，このクロススペクトルからサーペント型造波機で起した多方向不規則波の方向スペクトルを推定した。クロススペクトルの算定に当っては，造波信号の作成法として用いられているシングルサンメーション (single summation) 法とダブルサンメーション (double summation) 法の2つの手法で検討した。その結果では，両手法とも基本的には差がないことが判明した。ただし，目標スペクトルに近い波を発生させるためには，両手法とも非常に多くの成分波を用いて造波信号を作成しなければならない。例えば，ダブルサンメーション法の場合，位相拘束の影響を除くためには450程度の周波数成分波が必要となる。

ベイズモデル (BDM) を用いて方向スペクトルを推定して，方向スペクトルの空間的変動性を計算によって調べた。それによると，観測点が造波機中心線から造波板に平行に移動すると，方向分布形が主方向に対して非対称になることがわかった。

方向集中度パラメータ S_{max} の値が25の場合，実験で求めた方向分布形は計算で求めた分布形とよく一致するが，$S_{max}=10$ や75では，一致の度合が悪かった。これは，造波信号の作成に用いた周波数成分波の個数が少ないことに起因していると考えられる。

* 海洋水理部 波浪研究室長
** 海洋水理部 波浪研究室

Contents

1. Introduction

Real sea waves have the property of directional randomness as exhibited in an aerial photograph of short crested waves. Coastal engineers have wanted to reproduce directional random waves in their wave basins for accurate model tests. Because the multi-directional waves can, in principle, be expressed as the superimposition of various different oblique waves, a serpent-type wave generator which was originally developed for the generation of regular trains of oblique waves can be utilized for the generation of the short crested waves.

Since Salter[1] developed a system for generating directional waves by using a serpent-type wave generator, several hydraulic laboratories in the world have built their multi-directinal wave generators, as listed up in Ref. 2). We have also built a multi-directional wave generator of the transportable piston-type which consists of 35 wave-makers with segmented wave paddles 0.8 m wide.

Several papers[3)~6)] have been published on the characteristics of wave generator system and for model tests in directional waves, but a few papers[7),8)] have touched upon the characteristics of directional spectra of the short crested waves generated by the serpent-type wave generator. In the present paper, the properties of the regular trains of oblique waves generated by a wave generator are investigated by the numerical calculation of the formula of oblique waves derived theoretically, and the validity of the formula is confirmed by experiments. The cross-spectra of multi-directional waves expected in a wave basin are formulated by the application of the formula of oblique wave, and the directional spectra are computed from the cross-spectra by using the Bayesian model[9),10)]. The characteristics of the numerically obtained spectra are investigated by comparing them with those of experimentally obtained ones.

Recently, the arguments[11)~14)] on the synthesis of directional random waves have been raised. The arguments seem to conclude that the representation of directional random waves by the double summation model does not satisfy the ergodicity of the sea state because of phase locking between directional component waves. The present paper clarifies the cause of the phase-locking and presents a solution to solve it.

2. Theoretical Formula and Characteristics of Oblique Regular Waves

2.1 Formulation of waves generated by a single wave-maker

We assume that a single wave paddle of the width b moves periodically to and fro with a constant amplitude and that two stationary boards are extended semi-infinitely on both sides of the paddle, as shown in Fig. 1. In order to simplify the formulation of the waves generated by the motion of the paddle, the followings are assumed: 1) a non-viscous and incompressible fluid, 2) an irrotational fluid motion, 3) a uniform water depth, 4) a sufficiently small motion of the wave paddle, compared with the water depth and the wavelength, and 5) an impermeable bottom.

These assumptions make it possible to express the motion of a fluid by the velocity potential, and to neglect non-linear terms which appear in the boundary conditions at the water surface and the wave paddle. The linearized condition of

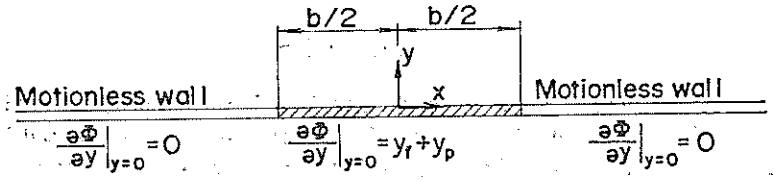

Fig. 1 Boundary conditions

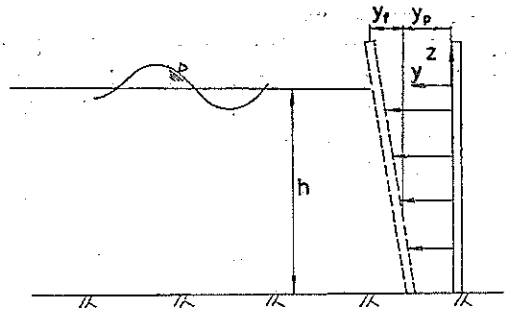

Fig. 2 Motion of a wave paddle

the paddle motion composed of two different movements of translation and rotation, as shown in Fig. 2, can be expressed as follows:

$$\left.\frac{\partial\Phi}{\partial y}\right|_{y=0}=\begin{cases}\sigma\left(Y_p+Y_f\dfrac{h+z}{h}\right)\cos\sigma t & (|x|\leq b/2)\\ 0 & (|x>b/2)\end{cases} \qquad (1)$$

where x and y represent the horizontal axes, as shown in Fig. 1, and z represents the vertical axis, positive upwards, as shown in Fig. 2. Furthermore, Φ, σ, t and h denote the velocity potential, the angular frequency of the paddle motion, the time and the still water depth, respectively, and the two different amplitudes of the translative motion and the rotational one at the still water level are represented by Y_p and Y_f, respectively.

The waves generated by a single paddle of finite width must propagate in radiating directions and their heights decrease with their propagation distance. Thus, they should satisfy the following Sommerfeld radiation condition at a point sufficiently distant from the center of the paddle:

$$\lim_{r\to\infty}\sqrt{r}\left(\frac{\partial\Phi}{\partial r}+\frac{k}{\sigma}\frac{\partial\Phi}{\partial t}\right)=0 \qquad (2)$$

where $r(=\sqrt{x^2+y^2})$ is the distance from the center of the paddle, and k $(=2\pi/L)$ denotes the wave number where L represents the wavelength. The wave number is the real solution of the following dispersion relation:

$$\sigma^2=gk\tanh kh \qquad (3)$$

The senior author[15] has derived the formula of the velocity potential which satisfies the mass conservation equation of

$$\frac{\partial^2\Phi}{\partial x^2}+\frac{\partial^2\Phi}{\partial y^2}+\frac{\partial^2\Phi}{\partial z^2}=0 \tag{4}$$

the linearized water surface conditions of

$$\frac{\partial^2\Phi}{\partial t^2}+g\frac{\partial\Phi}{\partial z}=0 \qquad (z=0) \tag{5}$$

and the bottom condition of

$$\frac{\partial\Phi}{\partial z}=0 \qquad (z=-h) \tag{6}$$

in addition to the paddle condition of Eq. (1) and the radiation condition of Eq. (2). The formula can be expressed as follows:

$$\begin{aligned}\Phi=&\left[\frac{\sigma}{k}(Y_p\alpha_p+Y_f\alpha_f)\frac{\cosh k(h+z)}{\sinh kh}\int_{-kb/2}^{kb/2}N_0(\sqrt{(kx-q)^2+(ky)^2})dq\right.\\&\left.-\sum_\nu\frac{\sigma}{\nu}(Y_p\beta_p+Y_f\beta_f)\frac{\cos\nu(h+z)}{\sin\nu h}\int_{-kb/2}^{kb/2}\frac{2}{\pi}K_0(\sqrt{(\nu x-q)^2+(\nu y)^2})dq\right]\cos\sigma t\\&-\frac{\sigma}{k}(Y_p\alpha_p+Y_f\alpha_f)\frac{\cosh k(h+z)}{\sinh kh}\int_{-kb/2}^{kb/2}J_0(\sqrt{(kx-q)^2+(ky)^2})dq\cdot\sin\sigma t\end{aligned} \tag{7}$$

where $J_0(x)$, $N_0(x)$ and $K_0(x)$ are the Bessel, Neumann and second kind modified Bessel functions of the 0-th order, respectively, and ν represents the real value solutions of

$$\sigma^2=-g\nu\tan\nu h \tag{8}$$

The coefficients of α_p and β_p, which indicate the transfer functions for wave generation by the paddle motion of translation, are given as

$$\alpha_p=\frac{\sinh^2 kh}{kh\left[1+\dfrac{\sinh 2kh}{2kh}\right]} \tag{9}$$

$$\beta_p=\frac{\sin^2 2\nu h}{\nu h\left[1+\dfrac{\sin 2\nu h}{2\nu h}\right]} \tag{10}$$

and the coefficients of α_f and β_f, which also indicate the transfer functions for the paddle motion of rotation, are given as

$$\alpha_f=\frac{[\sinh kh-(\cosh kh-1)/kh]\sinh kh}{kh\left[1+\dfrac{\sinh 2kh}{2kh}\right]} \tag{11}$$

$$\beta_f=\frac{[\sin\nu h+(\cos\nu h-1)/\nu h]\sin\nu h}{\nu h\left[1+\dfrac{\sin 2\nu h}{2\nu h}\right]} \tag{12}$$

The transfer functions expressed by Eqs. (9) and (11) are the same as those obtained by Biesel et al.[16] as the transfer functions for the piston-type and flap-type wave-makers, respectively, in a two-dimensional channel. The same formula of Eq. (7) has been derived by Dalrymple and Greenberg[17] independently.

By substituting Eq. (7) into the linearized dynamic condition at the water surface, the wave profile $\zeta(x, y, t)$ can be expressed as follows:

$$\zeta=(Y_p\alpha_p+Y_f\alpha_f)\Big[\sin\sigma t\int_{-kb/2}^{kb/2}N_0(\sqrt{(kx-q)^2+(ky)^2})dq$$
$$+\cos\sigma t\int_{-kb/2}^{kb/2}J_0(\sqrt{(kx-q)^2+(ky)^2})dq\Big]$$
$$+\sum_{\nu}(Y_p\beta_p+Y_f\beta_f)\sin\sigma t\int_{-\nu b/2}^{\nu b/2}\frac{2}{\pi}K_0(\sqrt{(\nu x-q)^2+(\nu y)^2})dq \qquad (13)$$

The first term in the right-hand side of Eq. (13) represents progressive waves which propagate radiatively and attenuate gradually, while the second term in the same side represents stationary waves which vanish at a point more distant than one wavelength from the wave paddle. Since the waves near the paddle are not significant in the present analysis, we ignore the stationary term and define the dimensionless wave height R_H as

$$R_H=H/2(Y_p\alpha_p+Y_f\alpha_f)$$
$$=\Big[\Big\{\int_{-kb/2}^{kb/2}J_0(\sqrt{(kx-q)^2+(ky)^2})dq\Big\}^2$$
$$+\Big\{\int_{-kb/2}^{kb/2}N_0(\sqrt{(kx-q)^2+(ky)^2})dq\Big\}^2\Big]^{1/2} \qquad (14)$$

Figure 3 shows an example of the computed distributions of the non-dimensional

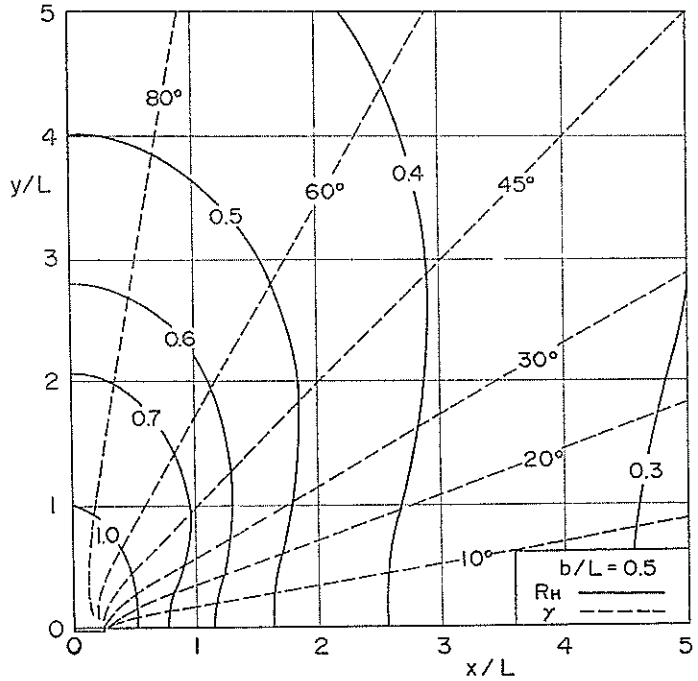

Fig. 3 Distribution of dimensiolness wave height R_H and wave propagation angle γ $(b/L=0.5)$

wave height R_H and the wave propagation angle γ for the case of $b/L=0.5$. The wave propagation angle is defined as the angle of the direction of the maximum fluid velocity measured from the positive axis of x. Each contour line of R_H indicated by the solid line in Fig. 3 shows the feature of an oval arc because of the concentration of wave energy in front of the paddle. The value of R_H on the radiative line from the center of the paddle decreases almost in inverse proportion to $\sqrt{r}$. On the other hand, the contour line of γ is extended radiatively except for in the vicinity with the paddle. The lines of γ do not cross perpendicularly with those of R_H. However, as the relative paddle width b/L becomes small, the crossing angle between the lines of γ and R_H approaches a right angle.

The validity of Eq. (7) has been confirmed by a comparison of the experiments and computations.[15]

2.2 Theoretical formula of oblique waves

The profile of the oblique wave generated by a serpent-type wave generator can be formulated by the linear superposition of Eq. (14). However, the phase difference of the motion between the adjacent wave paddles must be introduced into the formation of the oblique waves. The phase difference is given as $-kb\cos\theta$, on the assumption that the oblique waves propagating in the direction of the angle θ can be uniformly generated by a group of a large number of wave paddles each with the width of b, where the oblique angle θ is defined as that measured from the positive axis of x.

By using the above phase difference, the wave profile of the oblique wave is derived as the following form:

$$\zeta_{ob}=\sum_{i=-N_-}^{N_+}(Y_p\alpha_p+Y_f\alpha_f)\Big[\sin(\sigma t-ikb\cos\theta)\times\int_{(i-1/2)kb}^{(i+1/2)kb}N_0(\sqrt{(kx-q)^2+(ky)^2})dq\Big]+\cos(\sigma t-ikb\cos\theta)\int_{(i-1/2)kb}^{(i+1/2)kb}J_0(\sqrt{(kx-q)^2+(ky)^2})dq\Big] \tag{15}$$

where the term of the stationary wave in Eq. (14) is neglected. In Eq. (15), N_+ and N_- denote the numbers of the wave paddles in the positive and negative x-axis respectively. The total width of the paddles is represented as $(N_++N_-+1)b$.

When the value of b/L is infinitely small, the summational form of Eq. (15) can be transformed into an integral one. The dimensionless height R_H and the propagation angle γ of the oblique wave are defined in the manner same as in 2.1.

2.3 Characteristics of simulated oblique waves

In order to investigate the properties of oblique waves, computations are carried out for various values of the target angle θ under the condition of the individual paddle width of $b/L=0.32$, the total paddle width of $B/L=12.8$, and the uniform water depth of $h/L=0.64$. The above condition expressed in the non-dimensional values corresponds, as an example, to $b=0.5$ m, $B=20$ m, and $h=1.0$ m for the paddle motion with the period of $T=1.0$ s.

Figs. 4(a) and (b) show the variations of the wave propagation angle θ and the dimensionless wave height R_H, respectively, on the line of $y/L=4$. These variations are computed for the four target angles of 90°, 80°, 60° and 45°. The thin

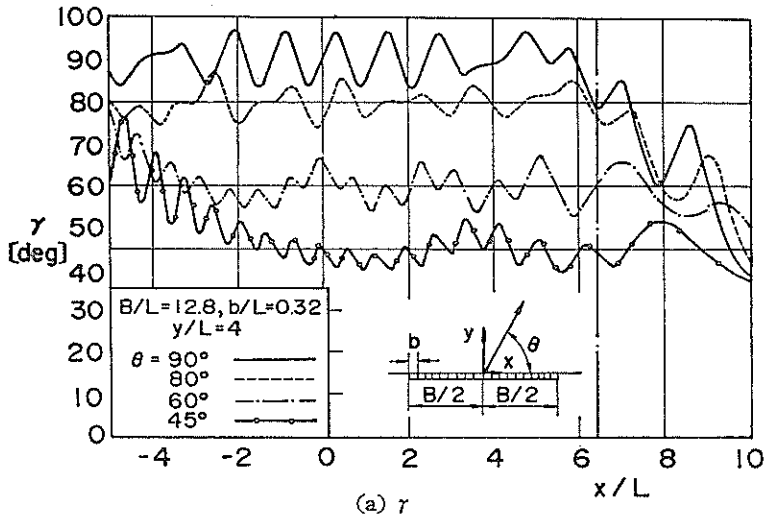

(a) γ

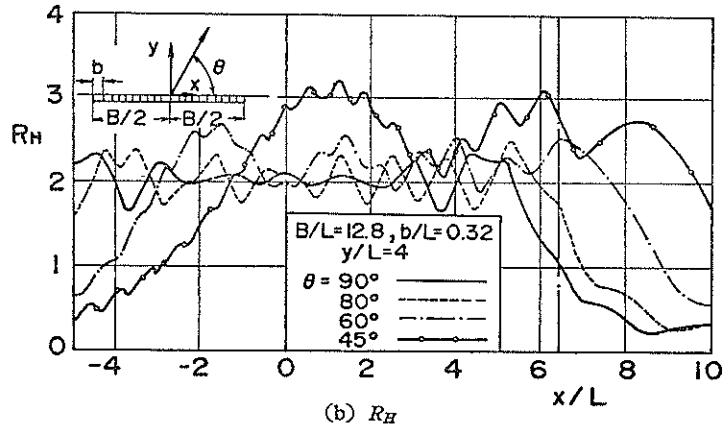

(b) R_H

Fig. 4 Variations of wave propagation angle γ and dimensionless wave height R_H for $y/L=4$

dash-dot lines parallel to the vertical axis of the figures indicates the outer end of the paddles.

In Fig. 4(a), each computed variation of the wave propagation angle shows the wavy feature which consists of undulations and ripples. The undulations become clear and the ripples attenuate, as the target angle deviates from the normal angle of 90°. The undulations and the ripples are not caused by the width of the individual paddle but by the finite total width of the paddles, because they appear even for the case of a normal angle of 90° where all paddles move in phase and the width of the individual paddle does not influence the generated wave. As the target angle deviates from 90°, the propagation angle of the oblique wave gradually approaches

the target one and the portion of almost uniform propagation angle becomes narrow. The deviation of the propagation angle from the target one is within 10° except for the approach portion to the target.

In Fig. 4(b) for the wave height, each variation of R_H also shows the wavy feature of undulations and ripples. As the target angle deviates from 90°, the undulations become clearly distinguishable, while the ripples become small. The undulations are a predominant factor for the variability of the wave height, especially in cases of large deviation like $\theta=60°$ and 45°. In the portion where the wave propagation angle is close to the target one, the value of R_H varies between 2.1 and 3.2 in case of $\theta=45°$, while it varies between 1.7 and 2.3 in case of $\theta=80°$. Thus, the average wave height in the above portion increases as the deviation of the target angle from 90° becomes large. This result indicates that when we generate oblique wave, the amplitude of the paddle motion calculated by the transfer function of wave generation for two-dimensional channel should be reduced by multiplying the calculated amplitude by $\sin\theta$.

Figure 4 clearly indicates that the generation of uniform train of oblique waves cannot be expected, even if the phase of the motion between the adjacent paddles is completely adjusted to the theoretically derived one. Although Fig. 4 clarifies that the undulations and the ripples are caused by the finiteness of the total paddle width, it is not clear whether their amplitudes depend upon the width of the individual paddle. Therefore, additional computations are carried out to investigate the dependency of the wave propagation angle and height upon the individual paddle width b.

Figures 5(a) and (b) show the variations of γ and R_H, respectively, for $\theta=60°$. The relative paddle width b/L adopted in the computations is 0, 0.32, 0.64 and 1.28, where the condition of $b/L=0$ means that the individual paddle widths are infinitesimal. The other conditions of the computations are the same as those of Fig. 4.

The wave propagation angle γ in Fig. 5(a) shows the wavy variation featured by undulations and ripples same as those in Fig. 4(a). The ripples attenuate as the relative paddle width b/L becomes small. This means that the amplitude of the ripples caused by the finiteness of the total paddle width depends on the value of b/L. The difference of the propagation angle between the two cases of $b/L=0$ and 0.32 is as small as to be negligible. In the portion of $-2<x/L<5$, where the value of γ is close to the target angle, the departure from the target is within 5° for above two cases. In the same portion, the value of γ for the case of $b/L=0.64$ varies around the target angle, having the maximum absolute difference of 10°, while in case of $b/L=1.28$ it largely varies around the angle quite different from the target. The relative paddle width of $b/L=1.28$ is too wide to generate the oblique waves with uniform propagation angle.

The dimensionless wave height R_H also shows a wavy variation with undulations and ripples, as shown in Fig. 5(b). The value of R_H approaches that for the case where $b/L=0$, as the relative width b/L becomes small. The dimensionless height in cases of $b/L=0.32$ and 0.64 is smaller than in the case of $b/L=0$ by 0.2 and 0.5 in maximum, respectively. The difference of the value of R_H between the two cases of $b/L=0$ and 1.28 is more than 1.5 because remarkable ripples appear in case of $b/L=1.28$. A paddle with the relative width of $b/L=1.28$ is no more useful for the generation of uniform trains of oblique waves.

The above discussion draws the following conclusions:

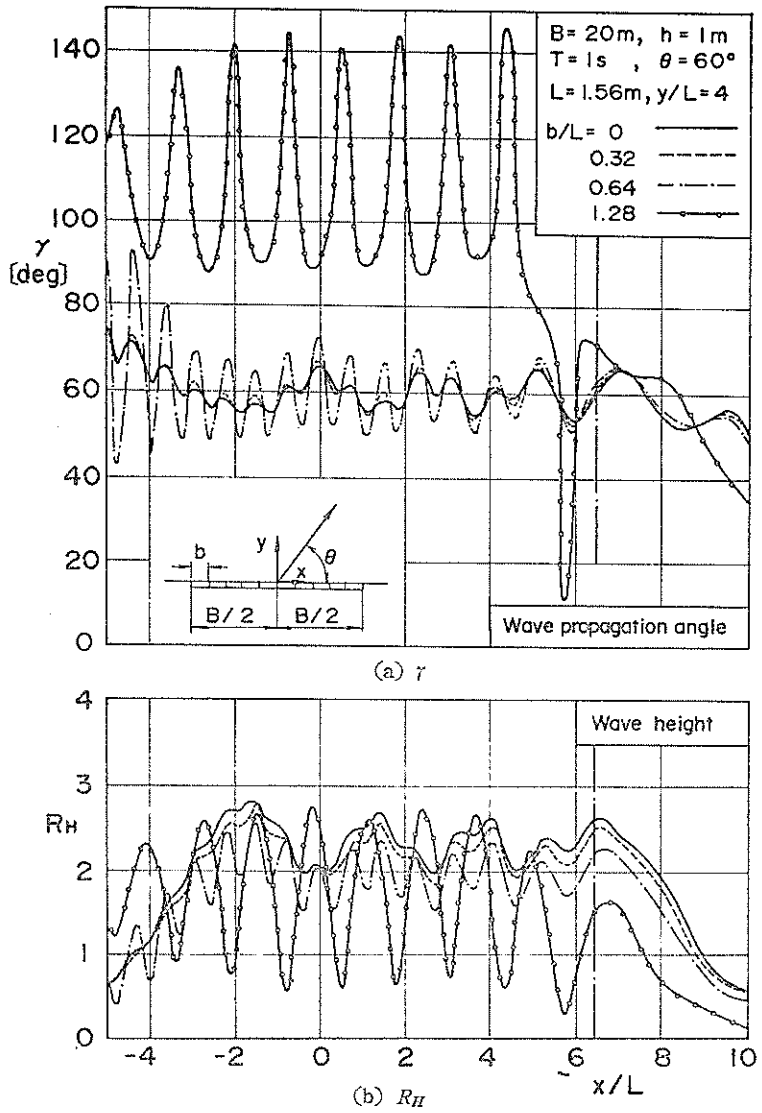

Fig. 5 Variations of wave propagation angle γ and dimensionless wave height R_H for various values of b/L

1) Even if the width of an individual wave paddles is made very small, it is impossible to eliminate the undulations and ripples which appear in the variations of wave propagation angle and height.
2) In order to generate uniform trains of oblique waves, it is important to reduce the individual paddle width, but it is not always necessary to reduce it up to very small quantity. The results of other various computations lead to the conclusion that a paddle width less than $b/L=0.5$ is sufficient to generate almost uniform trains of oblique waves.

3) The elongation of the total paddle width is important to eliminate the undulations and ripples, rather than the reduction of the individual paddle width.

3. Generation Method of Directional Random Waves and Characteristics of Theoretically Computed Directional Spectra

3.1 Generation method of directional random waves

It is reasonable to assume that directional random waves can be mathematically expressed as the linear superposition of a number of oblique component waves with different frequencies and propagation directions. As described in the previous chapter of 2, the oblique component wave can be generated by controlling phase differences between the motions of segmented wave paddles. For the generation of oblique wave by a serpent-type wave generator, the motion η_i of the i-th segmented wave paddle can be formulated as

$$\eta_i=\frac{a}{F}\sin(\sigma t-ikb\cos\theta+\varepsilon) \tag{16}$$

where a and θ represent the amplitude and the propagation direction of the target oblique wave, and F and ε denote the transfer function for the oblique wave generation and the phase lag between the oblique wave and the motion of the segmented wave paddle, respectively. The multiplication by $\sin\theta$ in Eq. (16) is made for the purposes of reducing the paddle motion because the oblique wave becomes larger than the normal wave, as described in 2.3. The transfer function F and the phase lag ε depend on the propagation direction θ, the wave angular frequency σ and the spatial point (x, y) of interest. Thus, the formulas for F and ε are very complicated. Therefore, we decided to utilize the transfer function for two-dimensional wave generation instead of that for the oblique wave generation. Consequently, the phase lag vanishes and the transfer function is given as the following form:
for piston-type wave-makers,

$$F=\frac{2\sinh^2 kh}{kh\left[1+\dfrac{\sinh 2kh}{2kh}\right]} \tag{17}$$

and for flap-type wave-makers,

$$F=\frac{2\sinh kh[\sinh kh-(\cosh kh-1)/kh]}{kh\left[1+\dfrac{\sinh 2kh}{2kh}\right]} \tag{18}$$

There are two different representations for directional random waves; one is the single summation model and the other is the double summation one. In the single summation model one frequency of an oblique component wave corresponds to one propagation direction. Thus, if the frequency is different, the propagation direction also differs to correspond to the frequency. On the other hand, in the double summation model one frequency of an oblique component wave has various different propagation directions. Thus, if we pick up the wave with a frequency, it involves a number of oblique waves with different propagation directions. The motion η_i of

the i-th segmented paddle can be formulated in these different representations as follows:

1) Single summation model

$$\eta_i=\sum_{n=1}^{N}\frac{a_n}{F_n}\sin(\sigma_n t-ik_n b\cos\theta_n+\varepsilon_n)\sin\theta_n \tag{19}$$

where a_n, σ_n, k_n, θ_n and ε_n represent the wave amplitude, the wave angular frequency, the wave number, the wave propagation angle and the phase difference, respectively. The subscript n denotes those of the n-th component wave. The value N indicates the number of the component waves, and the fuction F_n represents the transfer function expressed by Eq. (17) or (18) for two-dimensional wave generation. If the spectrum $S(f,\theta)$ $(=S(f)G(\theta;f))$ of directional random waves are given where $S(f)$ and $G(f;\theta)$ denote the frequency spectrum and the normalized angular spreading, the wave amplitude a_n is expressed by

$$a_n=\sqrt{2S(f_n)\delta f_n} \tag{20}$$

where δf_n denotes the small interval of frequency.

The representative frequency f_n of the n-th component wave can be calculated by the second moment of the frequency spectrum, and its approximate formula[18] is

$$f_n=\frac{1.007}{T_{1/3}}\{\ln[2N/(2n-1)]\}^{-1/4} \tag{21}$$

if the frequency spectrum of the Bretschneider-Mitsuyasu type expressed by Eq. (36) is employed.

The representative propagation angle θ_n must be distributed successfully by regarding the angular spreading $G(\theta;f)$ as a probability density function.

The phase difference ε_n is distributed uniformly as a random value between 0 and 2π.

2) Double summation model

$$\eta_i(t)=\sum_{n=1}^{N}\sum_{m=1}^{M}\frac{a_{nm}}{F_n}\sin(\sigma_n t-ik_n b\cos\theta_m+\varepsilon_{nm})\sin\theta_m \tag{22}$$

where a_{nm} and ε_{nm} represent the amplitude and the phase difference of the nm-th component wave, and θ_m is the propagation angle of the m-th wave direction. The subscripts n and m indicate those of the n-th frequency and the m-th direction. The values of N and M indicate the numbers of component waves in frequency and direction, respectively.

The wave amplitude a_{nm} is given as

$$a_{nm}=\sqrt{2S(f_n,\theta_m)\delta f_n\delta\theta_m} \tag{23}$$

where δf_n and $\delta\theta_m$ are small intervals of frequency and propagation angle.

The representative frequency f_n is calculated in a manner the same as that in the single summation model, and the representative angle θ_m is generally distributed uniformly between 0 to π at constant intervals. The phase lag ε_{nm} is given in the same manner as ε_n in the single-summation.

3.2 Theoretical analysis of cross-spectra

When individual paddles of the wave generator are moved as described in the

previous section of 3.1, the wave profiles at an arbitrary spatial point can be obtained theoretically. The simultaneous wave profiles at several points in a wave basin can be used to derive the covariance function $\phi_0(\tau; X, Y)$ defined by

$$\phi_0(\tau; X, Y)=\lim_{t_0\to\infty}\frac{1}{t_0}\int_{-t_0/2}^{t_0/2}\zeta(t; x, y)\zeta(t+\tau; x+X, y+Y)dt \tag{24}$$

where τ, X and Y represent the time lag and the spatial lags in x- and y-axis, respectively, at any two points. The cross-spectrum $\Phi_0(f; X, Y)$ is given as the following Fourier transform of $\phi_0(\tau; X, Y)$:

$$\Phi_0(f; X, Y)=\int_{-\infty}^{\infty}\phi_0(\tau; X, Y)e^{-i2\pi f\tau}d\tau \tag{25}$$

The cross-spectrum is often expressed in terms of its real and imaginary parts as

$$\Phi_0(f; X, Y)=C_0(f; X, Y)-iQ_0(f; X, Y) \tag{26}$$

where the real part $C_0(f; X, Y)$ is called the co-spectrum and the imaginary part $Q_0(f; X, Y)$ is called the quadrature-spectrum. If we obtain the cross-spectrum, we can calculate the directional spectrum by applying a reliable estimation method such as EMLM (Extended Maximum Likelihood Method) and BDM (Bayesian Directional Spectrum Method). The theoretical cross-spectrum differs by the two different representations of the single and double summations described in the previous section. Therefore, we will discuss the cross-spectrum obtained by each different representation.

(1) Cross-spectrum in the single summation model

When the segmented individual paddle moves as expressed by Eq. (19), the wave profiles at the point of (x, y) are formulated as

$$\begin{aligned}\zeta(x, y, t)=\sum_{n=1}^{N}\sum_{i=-N_-}^{N_+}\frac{a_n}{2}\{&N^*_{in}(x, y)\sin(\sigma_n t-ik_nb\cos\theta_n+\varepsilon_n)\\&+J^*_{in}(x, y)\cos(\sigma_n t-ik_nb\cos\theta_n+\varepsilon_n)\}\sin\theta_n\end{aligned} \tag{27}$$

where,

$$\left.\begin{aligned}N^*_{in}(x, y)&=\int_{(i-1/2)k_nb}^{(i+1/2)k_nb}N_0(\sqrt{(k_nx-q)^2+(k_ny)^2})dq\\J^*_{in}(x, y)&=\int_{(i-1/2)k_nb}^{(i+1/2)k_nb}J_0(\sqrt{(k_nx-q)^2+(k_ny)^2})dq\end{aligned}\right\} \tag{28}$$

By substitution of Eq. (27) into Eq. (24), the covariance function is obtained as

$$\begin{aligned}\phi_0(\tau; X, Y)=\sum_{n=1}^{N}\sum_{i=-N_-}^{N_+}\sum_{i'=-N_-}^{N_+}\frac{a_n^2}{4}[&N^*_{nii'}\cos\{\sigma_n\tau+(i-i')k_nb\cos\theta_n\}\\&+J^*_{nii'}\sin\{\sigma_n\tau+(i-i')k_nb\cos\theta_n\}]\end{aligned} \tag{29}$$

where,

$$\left.\begin{aligned}N^*_{nii'}&=N^*_{in}(x, y)N^*_{i'n}(x+X, y+Y)+J^*_{in}(x, y)J^*_{i'n}(x+X, y+Y)\\J^*_{nii'}&=J^*_{in}(x, y)N^*_{i'n}(x+X, y+Y)-N^*_{in}(x, y)J^*_{i'n}(x+X, y+Y)\end{aligned}\right\} \tag{30}$$

By Fourier transformation of the above function of Eq. (29) the co- and quadrature-spectra are given as

$$\left.\begin{aligned} C_0(f_n;\ X,\ Y)&=\frac{1}{4}S(f_n)\sum\sum\{N^*_{nii'}\cos\ [(i-i')k_nb\cos\theta_n]\\ &\quad+J^*_{nii'}\sin\ [(i-i')k_nb\cos\theta_n]\}\sin^2\theta_n\\ Q_0(f_n;\ X,\ Y)&=\frac{1}{4}S(f_n)\sum\sum\{N^*_{nii'}\sin\ [(i-i')k_nb\cos\theta_n]\\ &\quad-J^*_{nii'}\cos[(i-i')k_nb\cos\theta_n]\}\ \sin^2\theta_n\end{aligned}\right\}\qquad(31)$$

The co- and quadrature-spectra expressed by Eq. (31) are equivalent to those of uni-directional oblique wave generated serpent-type wave generator, because a discretely given wave frequency in the single summation model has only one wave propagation direction. Consequently, the directional spreading function calculated by Eq. (31) becomes the very sharp directional distribution as shown by the dirac δ-function, and the predominant direction θ_n of the angular spreading varies with a different run of random values calculated for the selection of the wave propagation direction θ_n. Therefore, we must employ the mean values of the co- and quadrature-spectra for the various runs of random values to select the wave propagation direction. Because the wave propagation angles are distributed according to the directional spreading function regarded as a probability density function, the mean values $\overline{C}_0(f_n;X,Y)$ and $\overline{Q}_0(f_n;X,Y)$ of the co- and quadrature-spectra converge to

$$\left.\begin{aligned} \overline{C}_0(f_n;\ X,\ Y)&=\frac{1}{4}S(f_n)\sum_{m=1}^{M_r}\sum_{i}\sum_{i'}\{N^*_{nii'}\cos\ [(i-i')k_nb\cos\theta_m]\\ &\quad+J^*_{nii'}\sin\ [(i-i')k_nb\cos\theta_m]\}\sin^2\theta_mG(\theta_m;\ f_n)\Delta\theta_m\\ \overline{Q}_0(f_n;\ X,\ Y)&=\frac{1}{4}S(f_n)\sum_{m=1}^{M_r}\sum_{i}\sum_{i'}\{N^*_{nii'}\sin\ [(i-i')k_nb\cos\theta_m]\\ &\quad-J^*_{nii'}\cos\ [(i-i')k_nb\cos\theta_m]\}\ \sin^2\theta_mG(\theta_m;\ f_n)\Delta\theta_m\end{aligned}\right\}\qquad(32)$$

where M_r and $\Delta\theta_m$ represent the number of the runs and the angular interval, respectively. The value of M_r needs to be no less than 30 to obtain a constant mean of co- and quadrature-spectra. If 30 representative frequencies are necessary to represent the frequency spectrum, the simulation of wave generation signals needs to be 900 wave components in frequency. If the angular spreading $G(\theta;f)$ depends upon the value of the frequency sensitively, more components may be necessary for the simulation. For a practical estimate of the directional spectrum, the means of the co- and quadrature-spectra are obtained by averaging the cross-spectra of different frequencies in the neighborhood of the representative frequency of f_n.

(2) Cross-spectrum in the double summation model

In the manner the same as the single summation model, the co- and quadrature-spectra are obtained as

$$\left.\begin{aligned} C_0(f_n;\ X,\ Y)&=\frac{1}{4}S(f_n)\sum_{m}\sum_{m'}\sum_{i}\sum_{i'}\{N^*_{nii'}\cos\ [(i\cos\theta_m-i'\cos\theta_{m'})k_nb\\ &\quad-(\varepsilon_{nm}-\varepsilon_{nm'})]+J^*_{nii'}\sin\ [(i\cos\theta_m-i'\cos\theta_{m'})k_nb-(\varepsilon_{nm}-\varepsilon_{nm'})]\}\\ &\quad\times\sqrt{G(\theta_m;\ f_n)\delta\theta_m}\sqrt{G(\theta_{m'};\ f_n)\delta\theta_{m'}}\sin\theta_m\sin\theta_{m'}\\ Q_0(f_n;\ X,\ Y)&=\frac{1}{4}S(f_n)\sum\sum\sum\sum\{N^*_{nii'}\sin\ [(i\cos\theta_m-i'\cos\theta_{m'})k_nb\\ &\quad-(\varepsilon_{nm}-\varepsilon_{nm'})]-J^*_{nii'}\cos\ [(i\cos\theta_m-i'\cos\theta_{m'})k_nb-(\varepsilon_{nm}-\varepsilon_{nm'})]\}\\ &\quad\times\sqrt{G(\theta_m;\ f_n)\delta\theta_m}\sqrt{G(\theta_{m'};\ f_n)\delta\theta_{m'}}\sin\theta_m\sin\theta_{m'}\end{aligned}\right\}\qquad(33)$$

Equation (33) indicates that the phase difference between two wave directions does not vanish in the representation of double summation model. The phase difference which remains in Eq. (33) is called phase locking. The values of the co- and quadrature-spectra vary largely, dependng on the phase lag given as uniform random value. The mean values of $\cos(\varepsilon_{nm}-\varepsilon_{nm'})$ and $\sin(\varepsilon_{nm}-\varepsilon_{nm'})$ for various runs of the phase lag converge to

$$\left.\begin{aligned}&\lim_{N_r\to\infty}\frac{1}{N_r}\sum_{p=1}^{N_r}\cos(\varepsilon_{nm}{}^{(p)}-\varepsilon_{nm'}{}^{(p)})=\begin{cases}1 & : m=m'\\ 0 & : m\neq m'\end{cases}\\&\lim_{N_r\to\infty}\frac{1}{N_r}\sum_{p=1}^{N_r}\sin(\varepsilon_{nmm}{}^{(p)}-\varepsilon_{nm'}{}^{(p)})=0\end{aligned}\right\}\qquad(34)$$

where N_r denotes the number of runs of random phase. Equation (34) has a satisfactory practical accuracy when the value of N_r is larger than 15. If the co- and quadrature-spectra given by Eq. (33) are averaged for more than 15 runs of the phase lag, they converge to the formulas given by Eq. (32). The averaging of $C_0(f_n;X,Y)$ and $Q_0(f_n;X,Y)$ for various runs of phase lags is equivalent to their averaging for various frequencies in the neighbor of the representative frequency of f_n. If 30 representative frequencies are necessary to represent the frequency spectrum, the simulation of wave generation signals needs to be 450 frequency components. Goda[19] has described in his simulations that at least 100 and 36 components in frequency and direction, respectively, are needed in the double summation model.

In the practical estimate of directional spectrum, we generally perform smoothing of the periodgram of the cross-spectra. The smoothing is equivalent to the above averaging of the co- and quadrature spectra.

Although several researchers[11)~14)] have emphasized that the representation of the double summation model gives undesirably wide distribution of wave energy spreading, the above examination reaches the conclusion that there is no fundamental difference between both models because they need avegaging of the co- and quadrature-spectra in frequency domain.

3.3 Characteristics of computed directional spectra

The cross-spectrum as described in 3.2 has the following relation to the directional spectrum:

$$S(f;\theta)=\frac{\alpha}{(2\pi)^2}\iint\Phi_0{}^*(f_n;X,Y)e^{i(k_nX\cos\theta+k_nY\sin\theta)}dXdY\qquad(35)$$

where $\Phi_0{}^*$is the conjugate function of the cross-spectrum Φ_0; i.e., $\Phi_0{}^*=C_0+iQ_0$ and α is a proportionality constant. The integration of Eq. (35) with respect to the spatial lags of X and Y is almost impossible to be performed because waves in the tank are not spatially uniform in their statistical meaning. Therefore, we must estimate the directional spectrum by using wave profiles simultaneously observed at a finite number of wave measurement points for a small area. Several estimation methods have been developed.

The Direct Fourier Transform (DFT) method developed by Barber[20] is one of the estimate methods, but this is not good to estimate the directional spectrum. Its directional resolution is rather dull and it yields negative values for the estimated spreading function in some ranges of direction.

A fairly common technique is the so-called maximum likelihood method (MLM) developed by Capon[21] for the analysis of seismic waves with a sensor array. It is designated to minimize the variance of the difference between the estimate and the true spectrum. Isobe and Kondo[22] have extended the method to apply to a set of various wave quantities like fluid velocities, surface slope and fluid pressure, and they have named their method as the extended maximum likelihood method (EMLM). Although these two methods of MLM and EMLM estimate the directional spreading function with a good directional resolution, the spreading function sometimes becomes divergent or cannot be obtained in case the determinant of the matrix of the cross-spectra is close or equal to 0.

Kobune and Hashimoto[23] have developed the maximum entropy method (MEM) to estimate the directional spectrum from the different three wave quantities of the wave profile and two horizontal fluid velocities. The directional resolution estimated by the method is better than the above other methods, but the limitation of a method valid only to three wave quantities reduces the applicability.

The new method of the Bayesian model (BDM) has been developed by Hashimoto[9),10] for estimating directional spectrum. It is designated that the directional spreading function is equivalent to the smooth regression curve in case the number of the parameters to be estimated is larger than the sample size. The concept of the Bayesian probability is introduced into the estimate of the regression curve. The Bayesian approach was originally proposed by Akaike[24] for the regression analysis. The results of numerical simulations confirm the validity of the method for the prediction of directional spreading, compared with the other estimate methods.

We employed BDM as the most reliable method for the estimate of the directional spectrum. The star array was adopted as the layout of the calculation points as shown in Fig. 6. The central point is set at the centroid of the equilateral triangular with a side length of $\sqrt{3}D$ (D=50 cm). The cross-spectra for the estimate of directional spectrum are calculated with Eq. (32).

We employed the following forms of Bretschneider-Mitsuyasu frequency spectrum and Mitsuyasu's angular spreading function as a target:

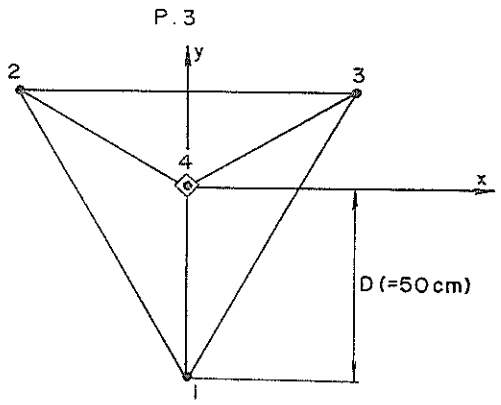

Fig. 6 Layout of computation points for estimate of directional spectra

$$S(f)=0.257H_{1/3}^2T_{1/3}(T_{1/3}f)^{-5}\exp\left[-1.03(T_{1/3}f)^{-4}\right] \tag{36}$$

and

$$G(\theta\,;\,f)=G_0\cos^{2S}\frac{\theta}{2} \tag{37}$$

where $H_{1/3}$ and $T_{1/3}$ represents the significant wave height and period, and G_0 the constant for the normalization given by

$$G_0=1/\int_{\theta_{\min}}^{\theta_{\max}}G(\theta\,;\,f)d\theta \tag{38}$$

The parameter S is related to the frequency and is given by the following form modified by Goda and Suzuki[25] by introducing the peak value of S, denoted as S_{max}, as the principal parameter for the purpose of engineering applications:

$$S=\begin{cases}S_{\max}(f/f_p)^5 & :f\leq f_p\\ S_{\max}(f/f_p)^{-2.5} & :f>f_p\end{cases} \tag{39}$$

where f_p denotes the spectral peak frequency and may be estimated from $T_{1/3}$ through the following relation:

$$f_p=1/(1.05T_{1/3}) \tag{40}$$

The calculation of directional spectra are performed for the wave generator which has been built in our institute[26]. It is composed of 35 wave-makers with a paddle width of 80 cm each. The calculations assume that no reflection occurs from the surrounding walls of the wave tank.

Figure 7 shows the variations of the angular spreading at the peak frequency to the relative paddle width b/L_p where L_p denotes the wavelength at the peak frequency. The computations are performed for the portion around the point of $x=0$ m and $y=5$ m. The computed angular spreading departs from the target of $S_{\max\ a}=10$ and becomes sharp as the value of b/L_p becomes large. The difference between the computed and target spreadings is within 0.1 at the peaks of the spreadings for

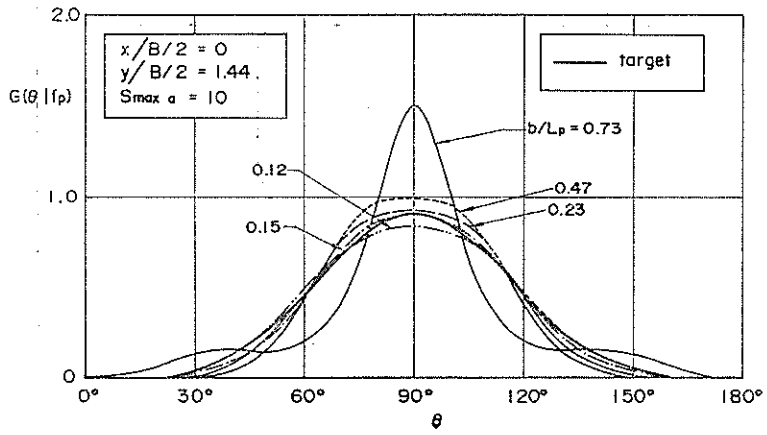

Fig. 7 Angular spreading for various relative widths of indiqidual paddle

$b/L_p<0.5$, while the difference becomes about 0.6 at the peak for case of $b/L_p=0.73$. The angular spreading for case of $b/L_p=0.15$ agrees well with the target. Thus, the relative paddle width b/L_p should be less than 0.5 for the generation of directional random waves with the angular spreading close to a target. Hereinafter, the discussion is made for $b/L_p=0.23$.

In order to investigate the reproducibility of the serpent-type wave generator, comparisons between simulated and target angular spreadings are made for several different values of S_{max}. Figure 8 shows the above comparisons for $S_{max}=10$, 25 and 75. The computation area is around the point of $x=0$ m and $y=5$ m. The computed spreading for $S_{max}=10$ is more gentle than the target around the peak, but their peaks agree well with each other. The computed spreadings for $S_{max}=25$ and 75 are sharper than the targets and their peaks are higher than those of the corresponding targets. The difference of the peak value between the computed and target spreadings increases as the value of S_{max} becomes large. Figure 9 shows similar comparisons in the area more distant from the paddles than the computation area of Fig. 8. Except for the feature that the peak value of the computed spreading for $S_{max}=10$ is smaller than that of the target by 0.04, the other features of the computed spreading in Fig. 9 are almost the same as those in Fig. 8.

Figure 10 shows the variations of the angular spreading for $S_{max}=10$ to the relative distance from the paddle. Although the distance is varied from $y/L_p=1.44$ to 4.33, corresponding to the distance of about 1.5 times the wavelength to a half total paddle width, the small difference among the angular spreadings is within 0.1. Thus, the distance from the paddles does not largely affect the angular spreading as far as it is less distant than the length of a half total paddle width.

In order to investigate the variation of the angular spreading to the transverse

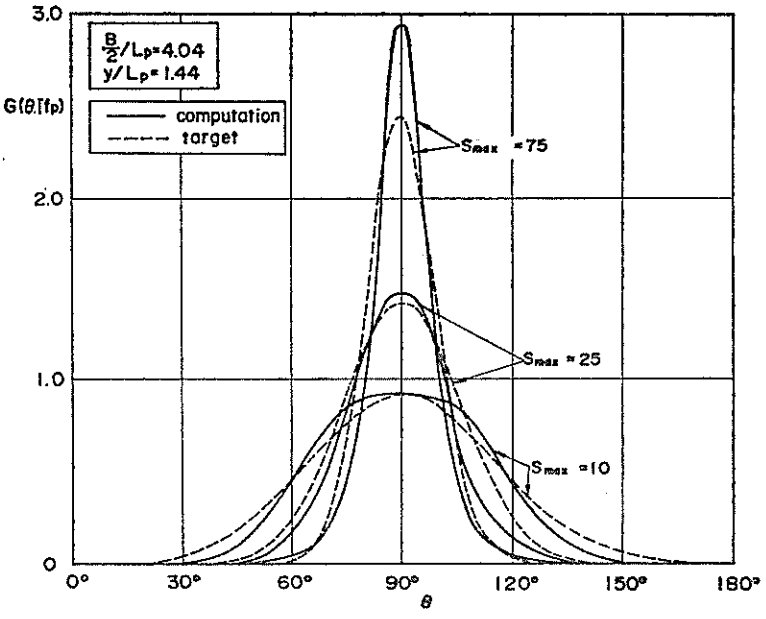

Fig. 8 Comparison of angular spreading between compution and target at $y/L_p=1.44$

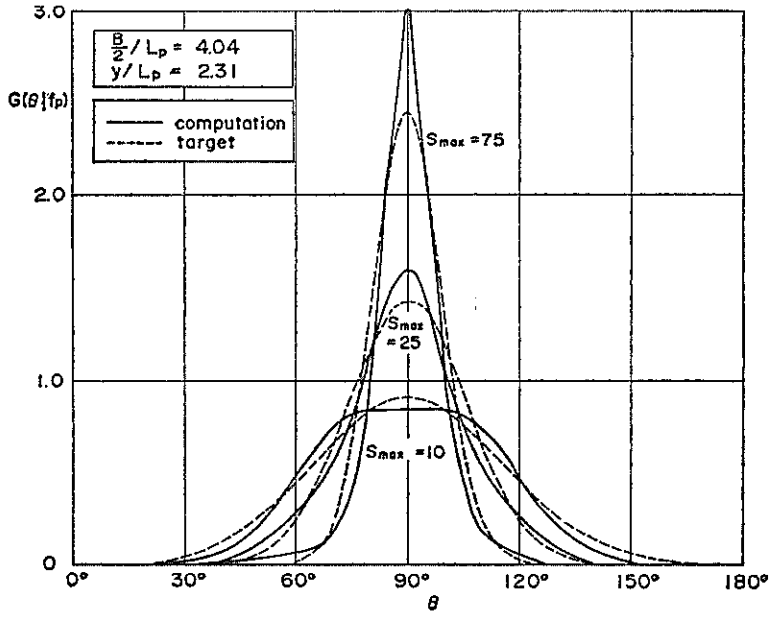

Fig. 9 Comparison of angular spreading between computation and target at $y/L_p=2.31$

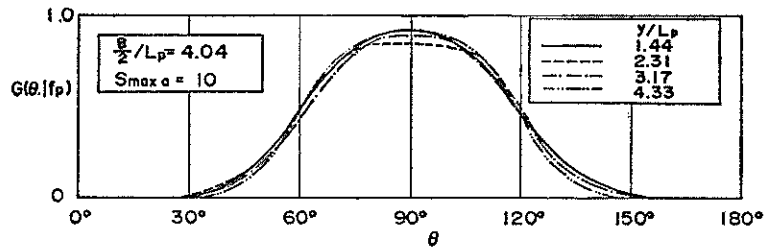

Fig. 10 Variations of angular spreading to the distance away from paddles

distance from the central line of $x=0$ m, several computations of the angular spreading are performed at different transverse distances. Figure 11 shows the comparisons between the computed and target angular spreadings at the point of $x=3$ m and $y=5$ m. In Fig. 11, the computed spreading for $S_{max}=10$ is distorted from the target and the peak appears at 80°, while the spreading for $S_{max}=75$ is almost same as that of the target and their peaks appear at the same angle of 90° to each other. Figure 12 shows a similar comparison at the point of $x=9$ m and $y=5$ m. Both peaks of the computed spreadings for $S_{max}=10$ and 75 appear at the angle of 90° the same as those of the targets, but their values are quite different from those of the corresponding targets. The peak value for $S_{max}=10$ is 1.6 times larger than that of the target, while the peak for $S_{max}=75$ is 0.7 times smaller than that of the target. This indicates that the reproduction of the target waves is difficult at such a point far away from the center line.

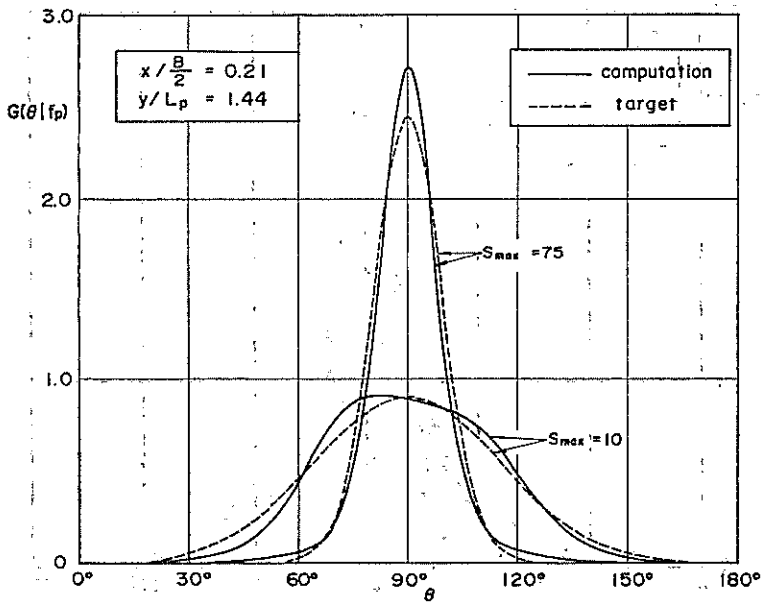

Fig. 11 Variation of angular spreading to transverse distance of $x/B/2=0.21$ from center line

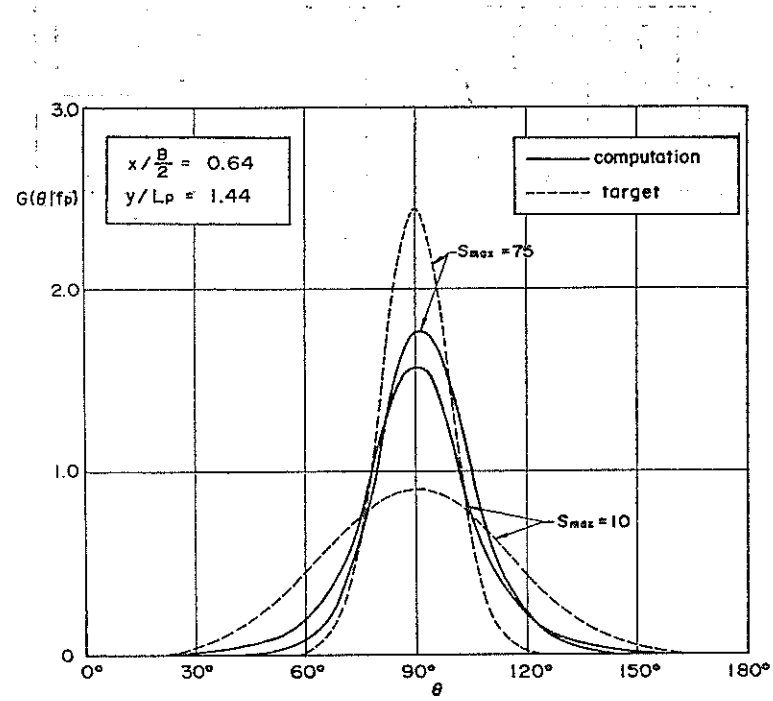

Fig. 12 Variation of angular spreading to transverse distance of $x/B/2=0.64$ from center line

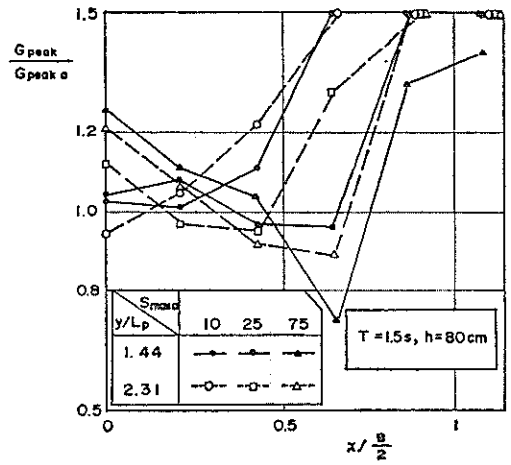

(a) Peak value of angular spreading

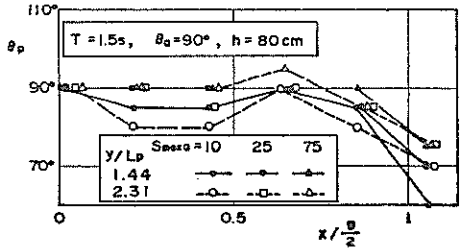

(b) Peak angle of angular spreading

Fig. 13 Variations of peak value of angular spreading and principal direction to transverse distance from center line

Figures 13(a) and (b) show the variations of the ratio of the peak value and the peak angle, respectively, to the transverse distance from the line of $x=0$. As shown in Fig. 13(a), the ratio of the peak value largely varies to the transverse distance. The peak angle shown in Fig. 13(b) does not vary largely, compared with the ratio of the peak value. Thus, we cannot expect the generation of directional random waves with uniform statistical characteristics. We must allow some degree of spatial variation for the directionality.

In the above, we discussed the directional spreading at the peak frequency. Here, we investigate the reproducibility of the whole forms of frequency spectrum and angular spreading in that they depend upon the frequency as expressed by Eqs. (36) and (37). Figure 14 shows the comparison between the computed and target frequency spectra. The simulated frequency spectrum for cases of $S_{max}=10$ and 75 shows a good agreement with the target, even if we compute the frequency spectrum by using the oblique wave formula of Eq. (27).

Figure 15 shows the comparison of the peak value G_{peak} of directional spreading at each frequency. For the case of $S_{max}=75$, the value of G_{peak} is larger at the peak frequency than that of the target and decreases more rapidly than the target, while for case of $S_{max}=10$ it is almost as same as that of the target, and decreases more gently than the target.

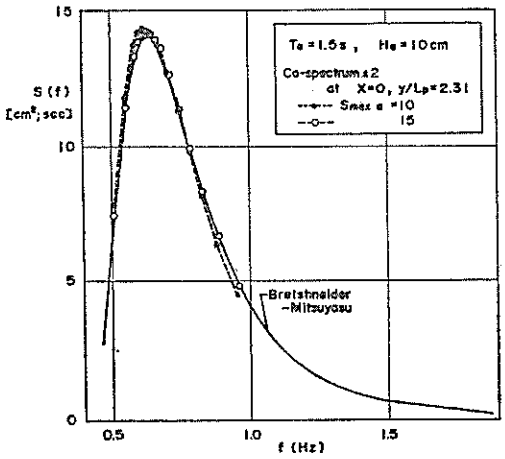

Fig. 14 Comparison of frequency spectrum between computation and target

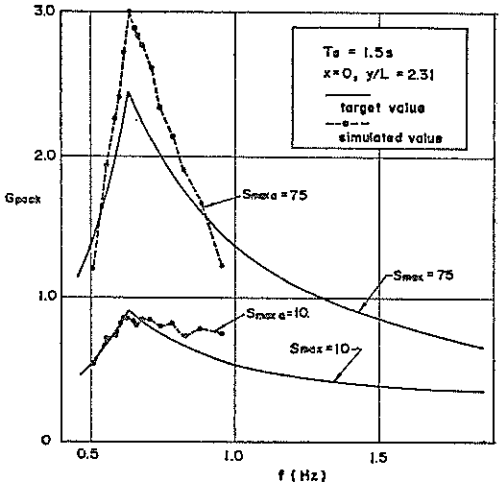

Fig. 15 Variation of peak value of angular spreading to frequency

4. Directional Random Waves Reproduced in a Laboratory Basin

4.1 Wave basin and serpent-type wave generator

(1) Wave basin

The serpent-type wave generator is installed in the wave tank which we call the short-crested wave tank. The short-crested wave tank is one of wave tanks inside the deep water experimental basin for offshore structures, as shown in Fig. 16, and is 24 m long, 36 m wide and 1.8 m deep. A serpent-type wave generator is installed along a side wall of 36 m wide.

Special concrete blocks with inclined slits are set along other side walls as wave absorber to prevent wave reflection from the walls because the wave reflection contaminates pure waves generated by the wave generator. The observed reflection coefficient of the wave absorbers is about 0.25 in minimum.

(2) Serpent-type wave generator[26]

The serpent-type wave generator at our institute is composed of 35 wave-makers. A set of five wave-makers is mounted on a same support and is transportable with the support. Figure 17 shows the sectional design of a wave-maker.

Each wave-maker has an independent wave paddle 80 cm wide and is driven by a DC motor. The rotation of the motor is translated to the reciprocal motion of a thrust beam through a screwed bar. The maximum stroke of the wave paddle is ±35 cm and the maximum drive speed is 60 cm/s.

The wave generator is operated by a remote controller through a micro-computer, which is also utilized for the simulation of wave generation signals. The digital signals are transmitted to each wave-maker by the direct memory access (DMA) after their conversion into analog signals. Figure 18 shows the system of the wave generator.

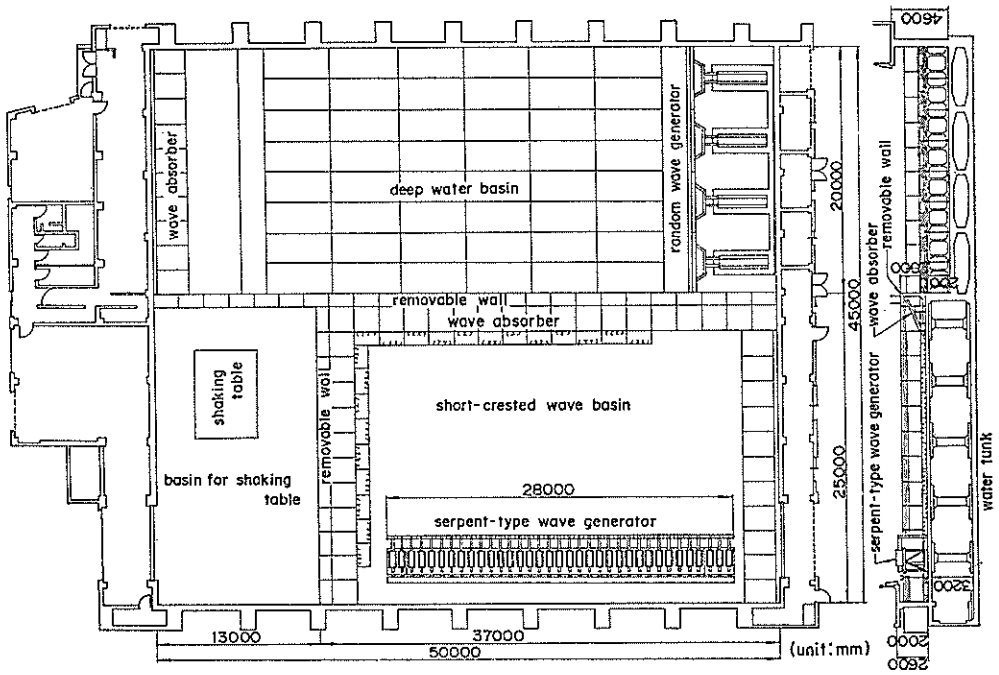

Fig. 16 Deep water experimental basin for offshore structure and location of short crested wave basin

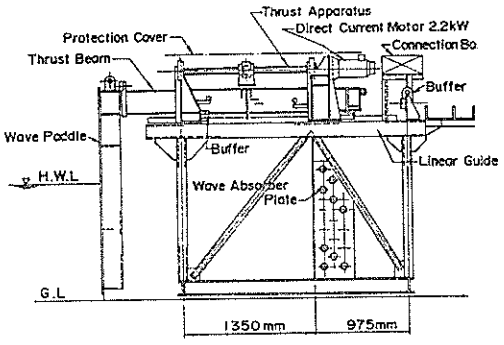

Fig. 17 Wave generator

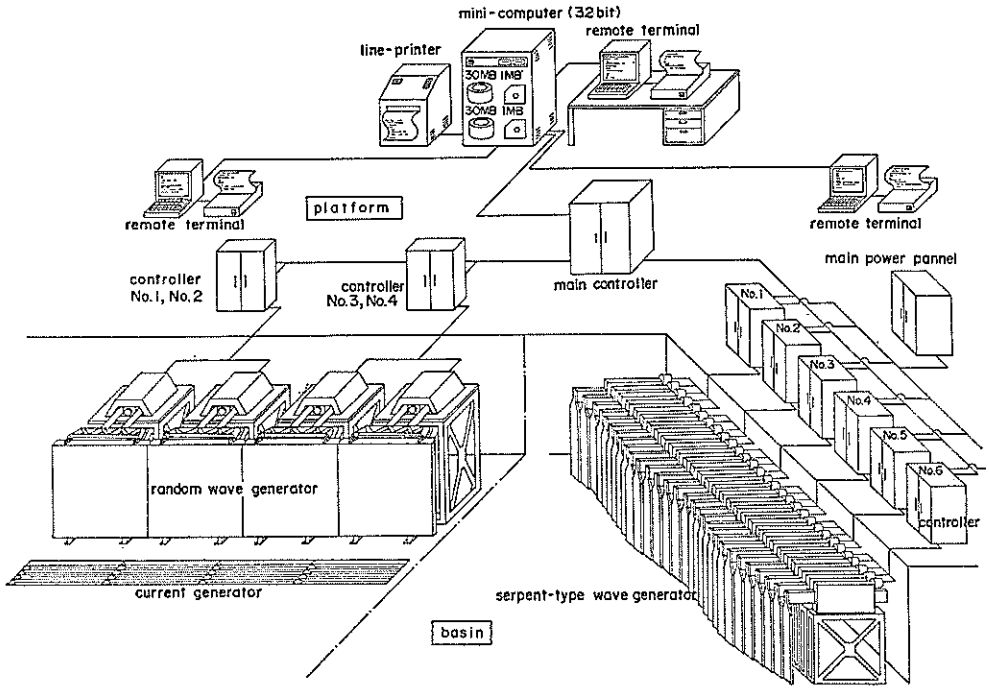

Fig. 18 Control system of wave generator

4.2 Experimental conditions

We performed two different kinds of experiments; one is on oblique regular waves to confirm the validity of the theoretically derived formula expressed by Eq. (15) and the other is on multi-directional waves to obtain their characteristics in the wave tank.

(1) Experiments on regular oblique waves

The purpose of the experiments is to confirm the validity of the theoretical formula of oblique waves given by Eq. (15). Considering the above purpose, only 10 central wave-makers are operated in order to strengthen the spatial variability of wave height.

Nine wave probes are installed in every distance of 1 m on the lines of $y=1$, 3 and 5 m away from the paddles. The experimental water depth is uniform 70 cm. The oblique wave angles are set to be 90°, 105°, 120° and 135° as the target angle. The target wave heights are adjusted to 5 cm for the period of 0.8 s, and 10 cm for the periods of 1.15 and 1.79 s.

(2) Experiments on multi-directional waves[27]

Generation signals of directional random waves are simulated under the double summation model as described in 3.1. The number of component waves is 30 in frequency and 30 in direction, and the total number of the components is 900. Although it is supposed that 30 frequency components is not enough to eliminate the effect of the phase locking as discussed in 3.2, we expected that the non-linearity of real water waves exhibits a smoothing effect among the component waves.

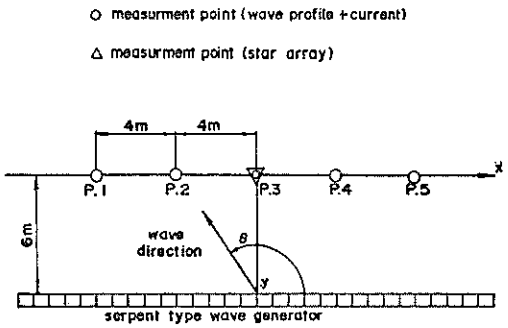

Fig. 19 Layout of wave probes

The uniform water depth in the experiments is 80 cm. Wave probes are placed as shown in Fig. 19. The star array of 4 wave gauges in the central part is mainly used to estimate the directional spectrum. The wave profile and two horizontal components of fluid velocity are simultaneously measured at other points. The targets of the significant wave height and period are 10 cm and 1.5 s, respectively.

4.3 Evaluation of theoretical formula of oblique waves by experiments

The wave propagation angle γ in the experiments can be obtained from the phase difference between two different wave profiles simultaneously measured at two

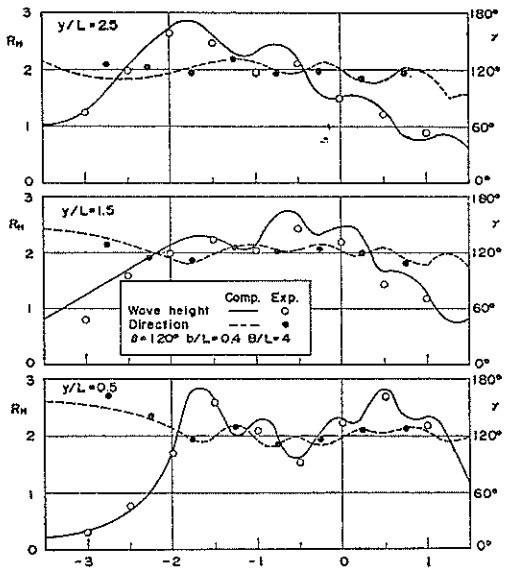

Fig. 20 Comparison of wave height and propagation direction between experiment and computation ($b/L=0.4$ and $\theta=120°$)

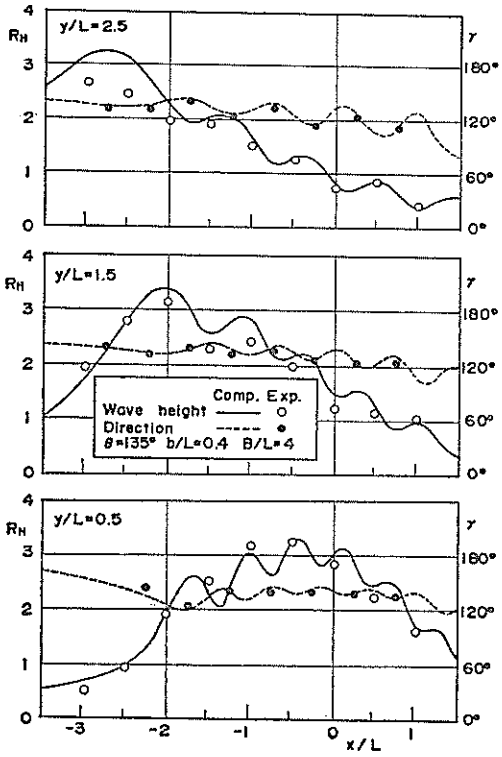

Fig. 21 Comparison of wave heign and propagation direction between experiment and computation ($b/L=0.4$ and $\theta=135°$)

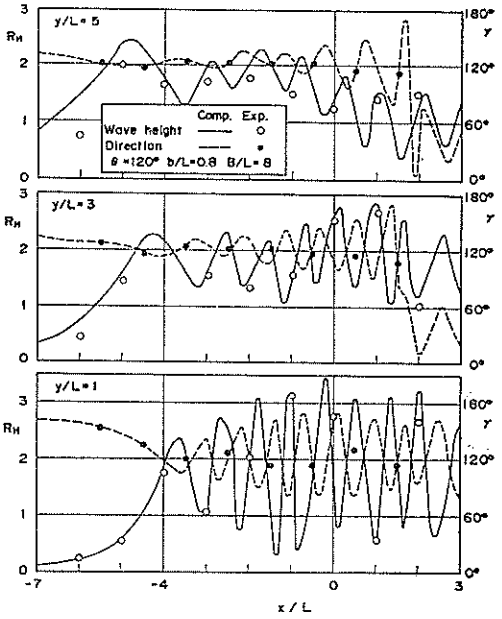

Fig. 22 Comparison of wave height and propagation direction betwee experiment and computation ($b/L=0.8$ and $\theta=120°$)

adjacent points. If the phase difference is represented by ε, the angle γ is calculated as the mean angle by

$$\gamma=\arctan(-\varepsilon/kl) \tag{41}$$

where l denotes the spatial distance between two adjacent points. On the other hand, the wave propagation angle in computation is calculated as the direction angle of maximum horizontal fluid velocity, as defined in 2.3.

Several examples of the comparisons of R_H and γ are shown in Figs. 20, 21 and 22. In these figures, the computed variation of R_H and γ are indicated by the solid and dashed lines, respectively, and the experimental values of R_H and γ are indicated by the small white and black circles, respectively.

Figures 20 and 21 show the comparisons for the case of the target propagation angles of $\theta=120°$ and 135°, respectively, and period of $T=1.15$ s. The solid lines of R_H show good agreement with the computed ones, though several experimental values are slightly different from the computed solid lines. The dashed line of γ shows wavy variations with small amplitudes, compared with those of R_H. The experimental values of γ agree quite well with the computed ones.

Figure 22 also shows the similar comparison for case of $\theta=120°$ and $T=0.8$ s. In

this case, the relative width b/L of an individual paddle is 0.8. Consequently the computed values of R_H and γ are much affected by the relative width and vary largely in short spatial distance. The peaks of the computed variations of R_H and γ appear at every interval of 0.8 m the same as the width of an individual paddle. The experimental values of R_H and γ show a fairly good agreement with the computed ones in spite of the large variations of the computed values.

Thus, a good agreement between the computation and the experiments confirm the validity of the theoretical formula of the oblique waves.

4.4 Comparison of theoretically simulated directional spectra with experimentally observed ones

The directional spectra of multi-directional waves in a laboratory basin are estimated by the two different methods of BDM and EMLM.

Figure 23 shows the comparison of the above two different methods for the directional waves with $S_{max}=50$ and the target principal direction of $\theta=90°$. The angular spreading estimated by EMLM shows a wide distribution of wave energy, compared with that by BDM. Consequently, the peak of the former angular spreading is lower than that of the latter. Some wave energy approaches from the opposite direction of 200° to 240°. The wave energy is supposed to be induced by reflection from the wave absorbers on the opposite side. The wave energy occupies 35% and 20% of total energy at peak frequency for EMLM and BDM, respectively. Considering that the reflection coefficient of the wave absorbers is about 0.3 and that the angular spreading estimated by BDM agrees with the target better than that by EMLM, BDM seems to be more valid than EMLM. Therefore, we made a comparison of the results estimated by BDM.

The comparisons between the analytical and experimental directional spreadings are made after the elimination of the reflected wave energy because the computation of angular spreading cannot include the effects of wave reflection.

Figure 24 shows the comparison of angular spreading at the peak frequency for case of the target value of $S_{max\ a}=10$. The computed angular spreading indicates

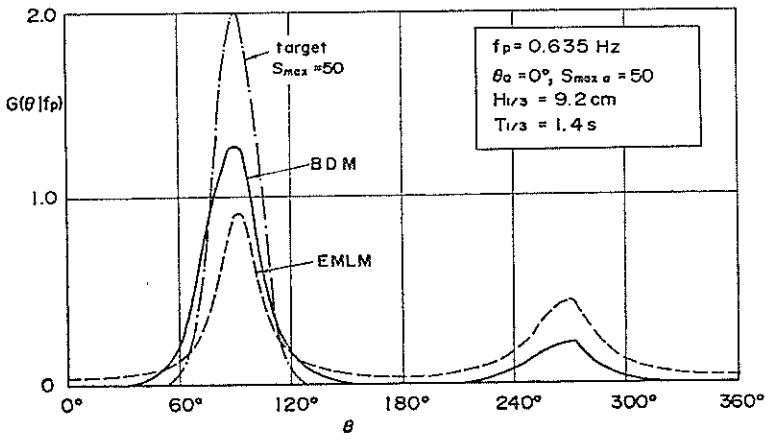

Fig. 23 Angular spreading estimated by BDM and EMLM

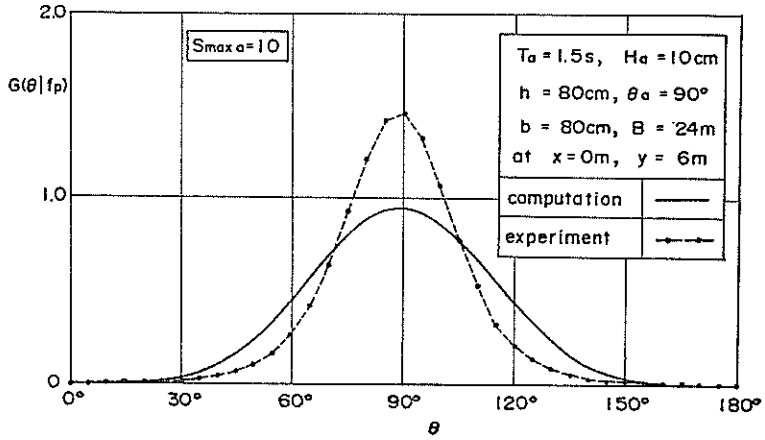

Fig. 24 Comparison of angular spreading for $S_{max}=10$

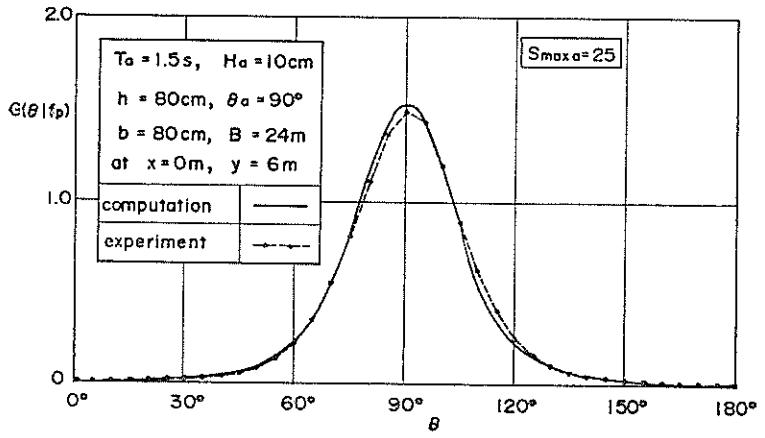

Fig. 25 Comparison of angular spreading for $S_{max}=25$

a wide distribution of wave energy, similar to the target, while the experimental spreading indicates concentrative distribution, which corresponds to that of $S_{max}=25$.

Figure 25 shows the similar comparison for $S_{max\,a}=25$. In the figure, the experimental spreading curve agrees quite well with the computed one.

In Fig. 26 for $S_{max\,a}=75$, the experimental directional spreading shows a wider distribution than the computed one. The experimental spreading corresponds to the distribution curve for $S_{max\,a}=30$.

The target principal angle in Fig. 27 for $S_{max\,a}=25$ was shifted to 95°. Both peaks of the experimental and computed angular spreading curves appear at the target angle of 95°, but the experimental directional spreading shows a wider distribution than the computed one and corresponds to the spreading for $S_{max\,a}=15$. Though the experimental directional spreading curve agrees well with the computed one in Fig. 25, the shift of the target angle by 5° causes wider distribution in the angular spreading.

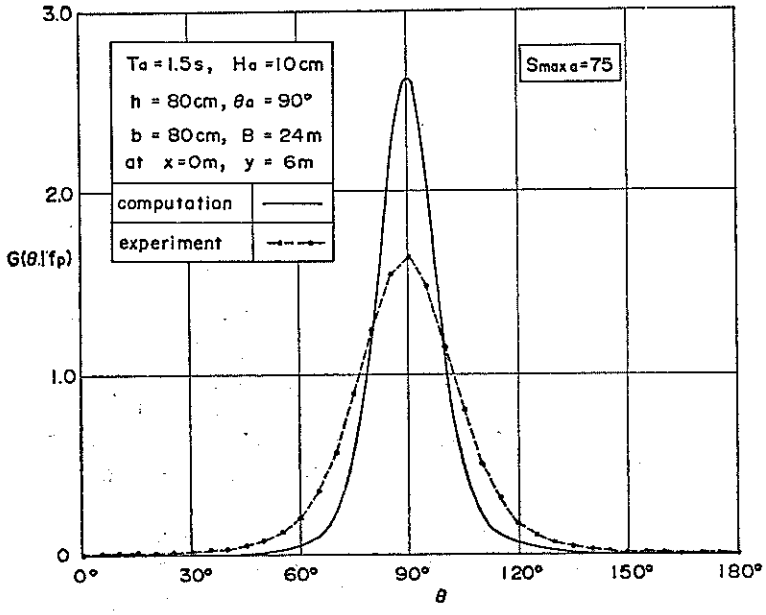

Fig. 26 Comparison of angular spreading for $S_{max}=75$

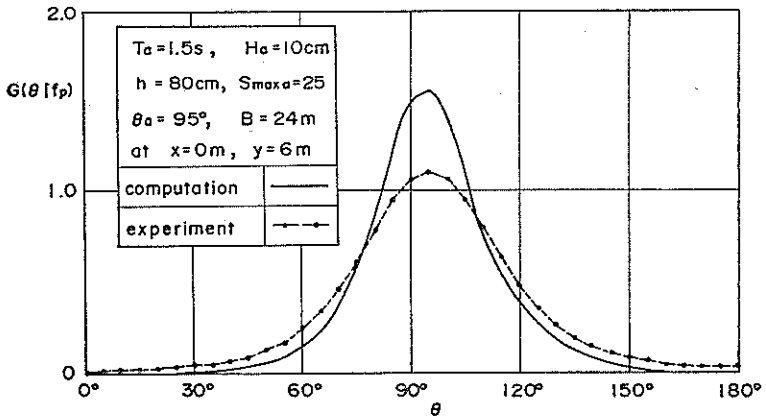

Fig. 27 Comparison of angular spreading of oblique waves for $S_{max}=25$

As discussed above, the experimental angular spreadings do not indicate the degree of concentration which corresponds to the target value of $S_{max\ a}$. This seems due to the insufficient number of the frequency components in the simulation of wave signals and a more detailed investigation is necessary for the suitable selection of the number of frequency components.

5. Conclusions

The present paper has discussed the properties of the oblique regular waves

and directional random waves generated by the serpent-type wave generator. In particular, the characteristics of angular spreading function have been discussed analytically and experimentally. The major findings of the study can be summarized as follow:

1. The theoretical formula of the oblique waves has been derived as the linear superimposition of the waves radiated by the motion of each wave paddle.
2. The height and propagation direction of the oblique waves predicted by the above formula agree quite well with the corresponding experimental values. Consequently, it has been confirmed that the formula is valid for the estimate of directional spectrum in a laboratory basin.
3. There are two different representations of directional random waves; one is the single summation model and the other is the double summation model. Both cross-spectra theoretically derived from the two different representations can be expressed by the same formula, for as long as the number of frequency components in the simulation of wave signals is sufficiently large. Therefore, it is concluded that there is no fundamental difference between the two different representations.
4. To eliminate the effect of phase locking in the double summation model, the number of frequency components needs to be more than 450.
5. The relative width b/L of individual paddle should be less than 0.5 to reproduce the directional random waves with the characteristics close to the target.
6. As far as a segmented wave generator of finite total width of paddles is used, we cannot expect to generate directional random waves with statistical properties quite the same as the target.
7. The directional spreading function varies spatially. In particular, when the observation points are transversely moved, the directional spreading curve is distorted from the target and becomes asymmetrical to the principal direction. We must allow some spatial variability of the directional spreading in the experiments.
8. For the value of the directional concentration parameter of $S_{max}=25$, the experimentally observed directional spreading function agrees well with the theoretically computed one, but for other values of S_{max} their agreement is not good. One of main causes of the disagreement seems to be due to the insufficient number of frequency components in the simulation of wave signals. We must investigate the suitable selection of the number of the frequency components in the simulation of wave generation signals in more detail.

(Received on November 18, 1987)

Acknowledgemens

The authors wishes to express their sincere gratitude to Dr. Yoshimi Goda, Director General of the Port and Harbour Research Institute, for his useful suggestions and discussions on the analysis of directional spectrum. A special dept of gratitude is owed to Mr. Noriaki Hashimoto, senior researcher of Hydraulic Engineering Division, for his lecturing accuracy of the estimate of directional spectrum and his presenting the program of BDM. The authors also express their thanks to Mr. Satoshi Honjou, member of the wave laboratory, for his assistance in performing the experiments and the computations.

References

1) SALTER, S. H.: Absorbing wave-makers and wide tanks, *Proc. of Conf. on Directional Wave Spectra Application, Univ. of California, Berkeley,* 1981, pp. 185~202.
2) MILES, M. D., P. H. LAURICH and E. R. FUNKE: A multi mode segmented wave generator for the NRC Hydraulic Laboratory, *Proc. of 21st American Towing Tank Conf., Washington, D.C.,* 1986.
3) AAGE, C. and E. SAND: Design and construction of the DHI 3-D wave basin, *Proc. of Symposium on Description and Modelling of Directional Seas, Tech. Univ., Denmark,* 1984, pp. B2-1~20.
4) OUTLAW, D. G.: A portable directional irregular waves generator for wave basin, *Proc. of Symposium on Description and Modelling of Directional Seas, Tech. Univ., Denmark,* 1984, pp. B3-1~8.
5) MYNETT, A. E., J. BOSMA and D. VAN VLIET: Effects of directional seas in coastal region, *Proc. of Symposium on Description and Modelling of Directional Seas, Tech. Univ., Denmark,* 1984, pp. B7-1~17.
6) BURCHARTH, H. F., S. P. K. NIELSEN and K. SCHAARUP-JENSEN: A three dimensional sea facility for deep and shallow water waves, *Proc. of Conf. Offshore Mechanics and Arctic Engng., OMAE, Tokyo,* Vol. 1, 1986, pp. 72~79.
7) NWOGU, O. U., E. P. D. MANSARD, M. D. MILES and M. ISAACSON: Estimation of Directional wave spectra by the maximum entropy method, *Proc. of IAHR-Seminar on Wave Analysis and Generation in Laboratory Basin, Lausanne,* 1987, pp. 363~376.
8) WU, Y. and R. A. DALRYMPLE: Analysis of wave fields generated by a directional wavemaker, *Coastal Engineering,* Vol. 11, 1987, pp. 241~261.
9) HASHIMOTO, H.: Estimation of directional spectra from a Bayesian approach, *Rept. of Port and Harbour Res. Inst.,* Vol. 26, No. 2, 1987, pp. 97~125 (*in Japanese*).
10) HASHIMOTO, N., K. KOBUNE and Y. KAMEYAMA: Estimation of directional spectrum from the Bayesian approach and its application to field data analysis, *Rept. of Port and Harbour Res. Inst.,* Vol. 25, No. 5, 1987, pp. 57~100.
11) FORRISTAL, G. Z.: Kinematics of directionally spread waves, *Proc. of Conf. on Directional Wave Spectra Applications, Univ. of California, Berkley,* 1981, pp. 129~146.
12) PINKSTAR, J. A.: Numerical modeling of directional seas, *Proc. of Symposium on Description and Modeling of Directional Seas, Tech. Univ., Denmark,* 1984, pp. C1-1~19.
13) SAND, S. E. and A. E. MYNETT: Directional wave generation and analysis, *Proc. of IAHR-Seminar on Wave Analysis and Generation in Laboratory Basin, Lausanne,* 1987, pp. 209~235.
14) JEFFERY, E. R.: Directional seas should be ergodic, *Applied Ocean Research,* Vol. 9, No. 4, 1987, pp. 186~191.
15) TAKAYAMA, T.: Theoretical properties of oblique waves generated by serpent-type wave-makers, *Rept. of Port and Harbour Res. Inst.,* Vol. 21, No. 2, 1982, pp. 3~48.
16) BIESEL, F., F. SUQUET and others: Les apparails generateurs de hoale en laboratoire, *La Houille Blanche,* Vol. 6, No. 2, 4, et 5, 1951 (*translated by St. Anthony Falls, Hyd. Lab., Univ. Minnesota, Rept. No. 39*).
17) DALRYMPLE, R. A. and M. GREENBERG: Directional wavemaker, *in Physical Modelling in Coastal Engng., R. A. Dalrymple, ed., Rotterdam: A. A. Balkema,* 1985, pp. 67~79.
18) GODA, Y.: Random seas and design of maritime structures, *Univ. of Tokyo Press,* 1985, p. 44.
19) GODA, Y.: Numerical experiments on statistical variability of ocean waves, *Rept. of Port and Harbour Res. Inst.,* Vol.. 16, No. 2, 1977, pp. 3~26.
20) BARKER, N. F.: The directional resolving power of an array of wave detectors, *Ocean*

Wave Spectra, Prentice-hall, Inc., 1965, pp. 460~471.

21) CAPON, J., R. J. GREENFIELD and R. J. KOLKER: Multi-dimensional maximum-likelihood processing of a large aperture seismic array, *Proc. IEEE*, Vol. 55, 1967, pp. 192~211.

22) ISOBE, M., K. KONDO and K. HORIKAWA: Extension of MLM for estimating directional spectrum, *Proc. of Symposium Description and Modelling of Directional Sea, Tech. Univ., Denmark*, 1984, pp. A6-1~15.

23) KOBUNE, K. and N. HASHIMOTO: Estimation of directional spectra from the maximum entropy principle, *Proc. of Offshore Mechanics and Arctic Engng., OMAE, Tokyo*, Vol. 1, 1986, pp. 80~85.

24) AKAIKE, H.: Likelihood and bayes procedure, Bayesian Statistics (*Bernard, J. M., De Groot, M. H. Du LindleyA., F. M. Smith eds.*), *University Press, Valencia*, 1980, pp. 143~166.

25) GODA, Y. and Y. SUZUKI: Computation of refraction and diffraction of sea waves with Mitsuyasu's directional spectrum, *Tech. Note of Port and Harbour Res. Inst.*, No. 230, 1975, 45p. (*in Japanese*).

26) TAKAYAMA, T., T. NAGAI and Y. GODA: Characteristics of serpent-type wave-maker and its control system, *Tech. Note of Port and Harbour Res. Inst.*, No. 509, 1984, 30p. (*in Japanese*).

27) TAKAYAMA, T. and H. HIRAISHI: Experimental characteristics of random waves generated by the serpent-type wave generator—The short-crested wave generator in the Offshore Structure Experimental Basin—, *Rept. of Port and Harbour Res. Inst.*, Vol. 26, No. 3, 1987, pp. 37~83 (*in Japanese*).

List of Symbols

a : amplitude of the target wave
a_n : amplitude of the n-th component wave
a_{nm} : amplitude of the nm-th component wave
B : total paddle width
b : width of an individual paddle
$C_0(f; X, Y)$: co-spectrum
F : transfer function for wave generation
F_n : transfer function of the n-th component wave in frequency
f : wave frequency
f_n : frequency of the n-th component wave
f_p : peak frequency
$G(\theta; f)$: angular spreading function
G_{peak} : peak value of $G(\theta; f)$
g : acceleration of gravity
H : wave height
$H_{1/3}$: significant wave height
h : water depth
$J_0(x)$: Bessel function of the 0-th order
J^*_{in} : $J^*_{in}=\int_{(i-1/2)k_nb}^{(i+1/2)k_nb} J_0(\sqrt{(k_nx-q)^2+(k_ny)^2})dq$
$J^*_{nii'}$: $J^*_{nii'}=J^*_{in}(x, y)N^*_{i'n}(x+X, y+Y)-N^*_{in}(x, y)J^*_{i'n}(x+X, y+Y)$
$K_0(x)$: second kind modified Bessel function of the 0-th order
k : wave number
k_n : wave number of the n-th frequency component wave

L : wavelength
L_p : wavelength at peak frequency
l : spatial distance between adjacent observation points
M : number of directional component waves
N : number of frequency component waves
$N_0(x)$: Neumann function of the 0-th order
N_+ : number of wave paddles in positive x-axis
N_- : number of wave paddles in negative x-axis

$N^*_{in}(x, y)$: $N^*_{in}(x, y)=\int_{(i-1/2)k_nb}^{(i+1/2)k_nb} N_0(\sqrt{(k_nx-q)^2+(k_ny)^2})dq$

$N^*_{nn'}$: $N^*_{nn'}=N^*_{in}(x, y)N^*_{i'n}(x+X, y+Y)+J^*_{in}(x, y)J^*_{i'n}(x+X, y+Y)$

$Q_0(f; X, Y)$: quadrature-spectrum
R_H : non-dimensional wave height
r : spatial distance to the point of interest
S : angular concentration parameter
$S(f)$: frequency spectrum
$S(f, \theta)$: directional spectrum
S_{max} : peak value of S at peak frequency
$S_{max\alpha}$: target value of S_{max}
T : wave period
$T_{1/3}$: significant wave period
t : time
X : spatial lag in x-axis
x : horizontal axis
Y : spatial lag in y-axis
Y_f : amplitude of paddle motion in flap type
Y_p : amplitude of paddle motion in piston type
y : horizontal axis
z : vertical axis, positive upwards

α_f : $\alpha_f=\dfrac{[\sinh kh-(\cosh kh-1)/kh]\sinh kh}{kh\left[1+\dfrac{\sinh 2kh}{2kh}\right]}$

α_p : $\alpha_p=\dfrac{\sinh^2 kh}{kh\left[1+\dfrac{\sinh 2kh}{2\,kh}\right]}$

β_f : $\beta_f=\dfrac{[\sin \nu h+(\cos \nu h-1)/\nu h]\sin \nu h}{\nu h\left[1+\dfrac{\sin 2\nu h}{2\nu h}\right]}$

β_p : $\beta_p=\dfrac{\sinh^2 kh}{\nu h\left[1+\dfrac{\sinh 2\nu h}{2\nu h}\right]}$

γ : wave propagation angle
δf_n : frequency interval of the n-th component wave
$\delta\theta_m$: directional interval of the m-th component wave
ε_n : phase lag of the n-th component wave
ε_{nm} : phase lag of the nm-th component wave
ζ : wave profile

ζ_{ob} : profile of oblique wave
η_i : motion of the i-th paddle
θ : wave propagation angle in target
θ_n : target propagation angle of the n-th component wave
ν : real solution of $\sigma^2=-g\nu\tan\nu h$
σ : angular frequency
τ : time lag
Φ : velocity potential
$\Phi_0(f;\ X,\ Y)$: cross-spectrum
$\phi_0(\tau;\ X,\ Y)$: covariance function